

Stream function – pressure virtual element methods for the Stokes–Darcy interface problem

Franco Dassi · Rekha Khot · David Mora · Andrés
E. Rubiano · Ricardo Ruiz-Baier

Received: date / Accepted: date

Abstract This paper introduces a novel Virtual Element Method (VEM) for the coupled Stokes–Darcy system in primal-primal form. In the free-flow Stokes domain, we implement a stream function formulation that inherently satisfies the incompressibility constraint and reduces computational cost. Across the interface, mass conservation, normal stress balance, and the Beavers–Joseph–Saffman slip condition are enforced to couple the biharmonic stream function equation with the Darcy’s pressure equation. Leveraging VEM’s ability to handle general polygonal meshes, the proposed method naturally accommodates irregular interface geometries without requiring remeshing or adaptive refinement. The accuracy of the method is validated through several numerical simulations that include applications to dead-end filtration, and network flow in bioartificial organs.

Keywords Stream function formulation · Interface problem · Coupled Stokes–Darcy · Virtual Element Methods · A priori error analysis

Mathematics Subject Classification (2020) 65N30 · 65N99 · 65Z05

1 Introduction

The coupling of free-flow with porous media flow is a fundamental challenge in fluid mechanics, with several applications ranging from groundwater hydrology and reservoir engineering to industrial filtration and biomedical modelling (see e.g. [15, 25, 28, 35, 49]). The interfacial coupling is achieved through continuity of normal velocities (mass conservation), balance of normal stresses, and the Beavers–Joseph–Saffman tangential slip condition [7, 50]. While more general frameworks account for porous media with cracks, and the incorporation of other linear and nonlinear equations in the coupled problem, such as Navier–Stokes, Brinkman and Forchheimer (see, e.g., [12, 24, 30, 33, 56]), the classical Stokes–Darcy system maintains the essential features of the interface mechanisms and remains the most important benchmark for modelling fluid-porous interfaces.

A wide range of primal and mixed Finite Elements (FEs), discontinuous Galerkin (dG), and Hybrid High–Order (HHO) methods have been developed for the Stokes–Darcy problem; a non-exhaustive list of representative references includes [2, 5, 6, 13, 16, 17, 19, 29, 32, 37, 52, 55]. Most of these approaches rely on velocity–pressure, velocity–pressure–pseudostress, or vorticity–pressure formulations in the Stokes

F. Dassi

Dipartimento di Matematica e Applicazioni, Università degli studi di Milano Bicocca, Via Roberto Cozzi 55, 20125, Milano, Italy. E-mail: Franco.Dassi@unimib.it

R. Khot

Department of Mathematics, Indian Institute of Technology Palakkad, Kanjikode 678623, Kerala, India. E-mail: RekhaKhot@iitpkd.ac.in

D. Mora

GIMNAP, Departamento de Matemática, Universidad del Bío-Bío, 4051381 Concepción, Chile; and CI²MA, Universidad de Concepción, Concepción, Chile. E-mail: DMora@ubiobio.cl

A. E. Rubiano · R. Ruiz-Baier

School of Mathematics, Monash University, 9 Rainforest Walk, Melbourne, VIC 3800, Australia. E-mail: Andres.RubianoMartinez@monash.edu, Ricardo.RuizBaier@monash.edu

region and either primal or mixed formulations in the Darcy region. These formulations require the design of compatible discrete spaces that satisfy appropriate inf-sup stability conditions and accurately enforce the interface coupling conditions. While conforming finite element methods often employ matching discretisations across the interface, dG and HHO formulations can naturally accommodate non-matching meshes through the weak enforcement of the coupling conditions.

Motivated by the need for geometric flexibility, recent years have also witnessed the development of Virtual Element Methods (VEMs) for the Stokes–Darcy problem on general polygonal meshes [43, 44, 53]. Originally introduced in [8], the VEM extends the finite element paradigm to general polygonal and polyhedral meshes while retaining many of its fundamental theoretical and computational properties. This flexibility makes VEM particularly attractive for interface problems, where complex geometries and non-matching meshes frequently arise.

In two-dimensional simply connected domains, however, the incompressibility constraint can be identically satisfied by introducing a scalar stream function [34], thereby eliminating the pressure variable from the Stokes equations. While this reformulation has been widely successfully exploited within the FE and dG frameworks [18, 21, 22, 31, 39, 42], its adaptation to virtual elements is more recent. In addition to reducing the number of Degrees of Freedom (DoFs), this well-known reformulation bypasses the need for inf-sup stable velocity–pressure pairs and yields a fourth-order problem for the stream function. Because the resulting formulation inherently requires $H^2(\Omega)$ conforming approximation spaces, C^1 -conforming VEMs are particularly well-suited, and several stream function formulations and associated pressure recovery algorithms have been successfully established for uncoupled Stokes and Navier–Stokes settings [1, 3, 45, 48]. However, their extension to the coupled Stokes–Darcy problem remains largely unexplored. This is precisely the gap we bridge in this paper.

Main contributions. The key novelties and contributions of this paper are summarised below:

- We develop a continuous analysis for the Stokes–Darcy interface problem in stream function – pressure formulation. This structure does not require inf-sup stability.
- We design a C^1 – C^0 lowest-order VEM discretisation for the stream function – pressure coupled Stokes–Darcy system. Such scheme involves only $3N_S + N_D + 4N_\Sigma$ DoFs, where N_S , N_D , and N_Σ are the number of interior vertices in the Stokes domain, Darcy domain, and on the interface, respectively.
- We conduct the a priori error analysis for the proposed VEM discretisation.
- We incorporate a new functionality in the open source object-oriented library `vem++` [26], allowing a straightforward implementation of interface problems through the class `vem::vemMesh2dDofFilter`.
- We provide several numerical experiments, confirming the theoretical findings and the applicability of the method.

Plan of the paper. This paper is organised in the following manner. The remainder of this section introduces preliminary notation and defines some classical functional spaces. Section 2 introduces the stream function – pressure formulation for the Stokes–Darcy interface problem. Next, the VEM spaces, DoFs, polynomial projection operators, interpolation estimates, and the discrete problem are provided in Section 3. Section 4 derives a priori error estimates for the discrete scheme. We show some numerical experiments in Section 5 to confirm our theoretical findings and Section 6 provides a summary of our conclusions and remaining open challenges.

Notation and preliminaries. Throughout this paper, $\Omega := \Omega_S \cup \Omega_D \subset \mathbb{R}^2$ is assumed to be a polygonal domain with Lipschitz continuous boundary $\Gamma := \partial\Omega$. For a vector function $\boldsymbol{\sigma} : \Omega \rightarrow \mathbb{R}^2$ and a scalar function $\phi : \Omega \rightarrow \mathbb{R}$, we define the vector gradient $\nabla\boldsymbol{\sigma} : \Omega \rightarrow \mathbb{R}^{2 \times 2}$, the scalar gradient $\nabla\phi : \Omega \rightarrow \mathbb{R}^2$, the vector divergence $\operatorname{div}\boldsymbol{\sigma} : \Omega \rightarrow \mathbb{R}$, the vector rotational $\operatorname{curl}\boldsymbol{\sigma} : \Omega \rightarrow \mathbb{R}$, the scalar rotational $\operatorname{curl}\phi : \Omega \rightarrow \mathbb{R}^2$, the vector Laplacian $\Delta\boldsymbol{\sigma} : \Omega \rightarrow \mathbb{R}^2$, the scalar Laplacian $\Delta\phi : \Omega \rightarrow \mathbb{R}$, and the Hessian matrix $\nabla^2\phi : \Omega \rightarrow \mathbb{R}^{2 \times 2}$ as $(\nabla\boldsymbol{\sigma})_{ij} := \partial_j\sigma_i$, $(\nabla\phi)_i := \partial_i\phi$, $\operatorname{div}\boldsymbol{\sigma} := \sum_i \partial_i\sigma_i$, $\operatorname{curl}\boldsymbol{\sigma} := \partial_1\sigma_2 - \partial_2\sigma_1$, $\operatorname{curl}\phi := (\partial_2\phi, -\partial_1\phi)^\top$, $(\Delta\boldsymbol{u})_i := \operatorname{div}(\nabla\boldsymbol{u})_i$, $\Delta\phi := \operatorname{div}(\nabla\phi)$, and $\nabla^2\phi := \nabla(\nabla\phi)$, respectively. Moreover, the following identities hold

$$\operatorname{div}(\operatorname{curl}(\phi)) = 0, \quad \operatorname{curl}(\phi) \cdot \boldsymbol{n} = \nabla\phi \cdot \boldsymbol{t}, \quad \text{and} \quad \operatorname{curl}(\phi) \cdot \boldsymbol{t} = -\nabla\phi \cdot \boldsymbol{n},$$

with \boldsymbol{n} and \boldsymbol{t} denoting the respective unit outward normal and tangential vectors with respect to Γ .

Given $s \geq 0$, we denote the usual Hilbert space of scalar and vector functions with domain Ω by $H^s(\Omega)$ and $\mathbf{H}^s(\Omega)$. The usual norm (resp. semi-norm) of $H^s(\Omega)$ is denoted by $\|\bullet\|_{s,\Omega}$ (resp. $|\bullet|_{s,\Omega}$). When $s = 0$, we define the Hilbert space $H^0(\Omega) := L^2(\Omega)$ with the usual inner product $(\bullet, \bullet)_\Omega$ (similarly for $\mathbf{L}^2(\Omega)$), while $L_0^2(\Omega)$ denotes the subspace of $L^2(\Omega)$ consisting of functions with zero mean over Ω . The trace space of $H^1(\Omega)$ is denoted by $H^{\frac{1}{2}}(\Gamma)$, and its dual space by $H^{-\frac{1}{2}}(\Gamma)$. The notation $(\bullet, \bullet)_\Gamma$ represents the duality pairing between $H^{-\frac{1}{2}}(\Gamma)$ and $H^{\frac{1}{2}}(\Gamma)$, induced by the $L^2(\Gamma)$ inner product.

Finally, C denotes a generic positive constant (which can have different values at its different occurrences) independent of the mesh size h and physical constants. Moreover, the notation $A \lesssim B$ indicates that for $A, B \geq 0$ we have that $A \leq CB$.

2 The model problem

In this section we introduce the stream function – pressure formulation for the Stokes–Darcy interface problem. The strong and weak formulations are derived using identities involving the **curl** operator. Finally, the well-posedness result is stated.

2.1 The classical Stokes–Darcy interface problem

Let Ω_S be a simply connected free-flow domain filled with a viscous incompressible fluid whose dynamics is governed by the velocity–pressure form of Stokes' equations

$$-\mu \Delta \mathbf{u} + \nabla p = \mathbf{f}, \quad \text{in } \Omega_S, \quad (1a)$$

$$\operatorname{div} \mathbf{u} = 0, \quad \text{in } \Omega_S, \quad (1b)$$

where $\mathbf{u} : \Omega_S \rightarrow \mathbb{R}^2$ denotes the velocity of the fluid and $p : \Omega_S \rightarrow \mathbb{R}$ the fluid pressure, both in the free-flow domain. In addition, $\mu > 0$ is the fluid viscosity and $\mathbf{f} : \Omega_S \rightarrow \mathbb{R}^2$ is a source/sink term. The boundary $\partial\Omega_S$ is the wall of the container separated into Γ_S and Σ such that $\partial\Omega_S = \Gamma_S \cup \Sigma$ and $\Sigma = \partial\Omega_S \setminus \Gamma_S$. We consider standard Dirichlet boundary conditions on Γ_S as follows

$$\mathbf{u} = \mathbf{0}, \quad \text{on } \Gamma_S. \quad (2)$$

On the other hand, consider a porous media Ω_D filled with fluid in the intrinsic pore space with pressure $\varphi : \Omega_D \rightarrow \mathbb{R}$ satisfying Darcy's Law

$$\operatorname{div}(-\kappa \nabla \varphi) = g, \quad \text{in } \Omega_D. \quad (3)$$

Here, $\kappa > 0$ is the hydraulic conductivity and $g : \Omega_D \rightarrow \mathbb{R}$ is another source/sink term and we assume that $\int_{\Omega_D} g = 0$. Similarly, the boundary $\partial\Omega_D$ fulfils the splitting $\Gamma_D \cup \Sigma$, with $\Sigma = \partial\Omega_D \setminus \Gamma_D$. In this case, no flux is prescribed in the following way

$$(-\kappa \nabla \varphi) \cdot \mathbf{n}_D = 0, \quad \text{on } \Gamma_D, \quad (4)$$

where \mathbf{n}_D is the unit outward normal vector with respect to Γ_D . Finally, we focus on the remaining portion of the boundary, the interface $\Sigma := \partial\Omega_S \cap \partial\Omega_D$, where the transmission conditions are

$$\mathbf{u} \cdot \mathbf{n}_\Sigma = (-\kappa \nabla \varphi) \cdot \mathbf{n}_\Sigma, \quad \text{on } \Sigma, \quad (5a)$$

$$-(\mu \nabla \mathbf{u} - p \mathbb{I}) \mathbf{n}_\Sigma \cdot \mathbf{n}_\Sigma = \varphi, \quad \text{on } \Sigma, \quad (5b)$$

$$-(\mu \nabla \mathbf{u} - p \mathbb{I}) \mathbf{n}_\Sigma \cdot \mathbf{t}_\Sigma = \alpha \frac{\mu}{\sqrt{\kappa}} \mathbf{u} \cdot \mathbf{t}_\Sigma, \quad \text{on } \Sigma. \quad (5c)$$

The third equation (5c) above is known as the Beavers–Joseph–Saffman transmission condition, in which the parameter α refers to the slip rate coefficient, the quotient $\mu/\sqrt{\kappa}$ represents the effective interfacial friction coefficient and $\mathbb{I} \in \mathbb{R}^{2 \times 2}$ is the identity matrix. In particular, we fix \mathbf{n}_Σ as the outward (resp. inward) unit normal vector with respect to $\partial\Omega_S$ (resp. Ω_D) when seen on Σ . A sketch of the computational domain highlighting the boundary configuration and interface is shown in Fig. 1(a).

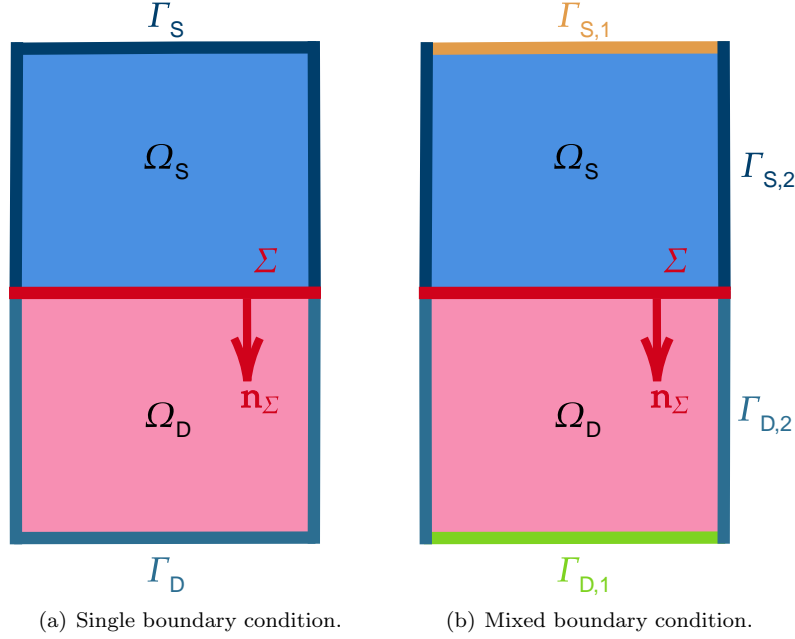


Fig. 1 Sketch of the computational domain and possible boundary configuration.

Remark 2.1 It is possible to consider various combinations of boundary conditions on Ω_S and Ω_D , provided they are compatible with the transmission conditions (5). For example, one can impose full Neumann conditions on Γ_S and full Dirichlet conditions on Γ_D , namely

$$(\mu \nabla \mathbf{u} - p \mathbb{I}) \mathbf{n}_S = \mathbf{0}, \quad \text{on } \Gamma_S, \quad (6a)$$

$$\varphi = 0, \quad \text{on } \Gamma_D, \quad (6b)$$

which is consistent with (5b). More generally, non-homogeneous and/or mixed boundary conditions may also be considered, as long as the conditions (2) and (4) (or alternatively (6a) and (6b)) are compatible. Some examples are given below: for $z_{D,2} \in H^{-\frac{1}{2}}(\Gamma_{S,2} \cup \Gamma_{D,2})$ and $\varphi_{D,2} \in H^{\frac{1}{2}}(\Gamma_{S,2} \cup \Gamma_{D,2})$, Fig. 1(b) illustrates the following configuration of the boundary sections $\Gamma_{S,1}$, $\Gamma_{S,2}$, $\Gamma_{D,1}$, and $\Gamma_{D,2}$

$$\begin{aligned} (\mu \nabla \mathbf{u} - p \mathbb{I}) \mathbf{n}_{S,1} &= \mathbf{0}, & \text{on } \Gamma_{S,1}, & \mathbf{u} = \mathbf{0}, & \text{on } \Gamma_{S,1}, \\ \mathbf{u} &= z_{D,2} \mathbf{n}_{S,2}, & \text{on } \Gamma_{S,2}, & (\mu \nabla \mathbf{u} - p \mathbb{I}) \mathbf{n}_{S,2} &= \varphi_{D,2} \mathbf{n}_{S,2}, & \text{on } \Gamma_{S,2}, \\ \varphi &= 0, & \text{on } \Gamma_{D,1}, & (-\kappa \nabla \varphi) \cdot \mathbf{n}_{D,1} &= 0, & \text{on } \Gamma_{D,1}, \\ (-\kappa \nabla \varphi) \cdot \mathbf{n}_{D,2} &= -z_{D,2}, & \text{on } \Gamma_{D,2}, & \varphi &= -\varphi_{D,2}, & \text{on } \Gamma_{D,2}. \end{aligned}$$

(Case 1) (Case 2)

In view of the boundary conditions (2) and (4), we define the following Hilbertian functional space

$$\mathbf{H}_{\Gamma_S}^1(\Omega_S) := \{\mathbf{v} \in \mathbf{H}^1(\Omega_S) : \mathbf{v} = \mathbf{0} \text{ on } \Gamma_S\}.$$

We multiply the governing equations by appropriate test functions, integrate by parts, and apply (5) to arrive at the weak formulation: given $\mathbf{f} \in \mathbf{L}^2(\Omega_S)$ and $g \in L_0^2(\Omega_D)$, find $(\mathbf{u}, p, \varphi) \in \mathbf{H}_{\Gamma_S}^1(\Omega_S) \times L^2(\Omega_S) \times H^1(\Omega_D)$ such that

$$\mu \int_{\Omega_S} \nabla \mathbf{u} : \nabla \mathbf{v} - \int_{\Omega_S} p \operatorname{div} \mathbf{v} + \frac{\alpha \mu}{\sqrt{\kappa}} \int_{\Sigma} (\mathbf{u} \cdot \mathbf{t}_{\Sigma})(\mathbf{v} \cdot \mathbf{t}_{\Sigma}) + \int_{\Sigma} \varphi \mathbf{v} \cdot \mathbf{n}_{\Sigma} = \int_{\Omega_S} \mathbf{f} \cdot \mathbf{v}, \quad \forall \mathbf{v} \in \mathbf{H}_{\Gamma_S}^1(\Omega_S), \quad (7a)$$

$$\int_{\Omega_S} q \operatorname{div} \mathbf{u} = 0, \quad \forall q \in L^2(\Omega_S), \quad (7b)$$

$$-\kappa \int_{\Omega_D} \nabla \varphi \cdot \nabla \psi + \int_{\Sigma} \mathbf{u} \cdot \mathbf{n}_{\Sigma} \psi = - \int_{\Omega_D} g \psi, \quad \forall \psi \in H^1(\Omega_D). \quad (7c)$$

2.2 The stream function – pressure interface formulation

Motivated by the incompressibility condition provided in (1b), we define the spaces

$$\mathbf{Z} := \{\mathbf{v} \in \mathbf{H}_{\Gamma_S}^1(\Omega_S) : \operatorname{div} \mathbf{v} = 0\} \quad \text{and} \quad \mathbf{H}_{\Gamma_S}^2(\Omega_S) = \{\xi \in \mathbf{H}^2(\Omega_S) : \xi = 0 \text{ and } \nabla \xi \cdot \mathbf{n}_S = 0 \text{ on } \Gamma_S\}.$$

By the stream function representation (see [34, Chap. I, Sect. 5.2 and Chap. IV, Sect. 2.2]), for any $\mathbf{u} \in \mathbf{Z}$ there exists $\chi \in \mathbf{H}^2(\Omega_S) \setminus \mathbb{R}$ such that $\mathbf{u} = \mathbf{curl} \chi$. This identification allows us to arrive at the following stream function – pressure weak formulation for the Stokes–Darcy interface problem: given $\mathbf{f} \in \mathbf{L}^2(\Omega_S)$ and $g \in L_0^2(\Omega_D)$; find $(\chi, \varphi) \in \mathbf{H}_{\Gamma_S}^2(\Omega_S) \times \mathbf{H}^1(\Omega_D)$ such that

$$\mu \int_{\Omega_S} \nabla^2 \chi : \nabla^2 \xi + \frac{\alpha \mu}{\sqrt{\kappa}} \int_{\Sigma} (\nabla \chi \cdot \mathbf{n}_{\Sigma})(\nabla \xi \cdot \mathbf{n}_{\Sigma}) + \int_{\Sigma} \varphi \nabla \xi \cdot \mathbf{t}_{\Sigma} = \int_{\Omega_S} \mathbf{f} \cdot \mathbf{curl} \xi, \quad \forall \xi \in \mathbf{H}_{\Gamma_S}^2(\Omega_S), \quad (8a)$$

$$-\kappa \int_{\Omega_D} \nabla \varphi \cdot \nabla \psi + \int_{\Sigma} \psi \nabla \chi \cdot \mathbf{t}_{\Sigma} = - \int_{\Omega_D} g \psi, \quad \forall \psi \in \mathbf{H}^1(\Omega_D). \quad (8b)$$

We now define the bilinear forms $a(\bullet, \bullet) : \mathbf{H}_{\Gamma_S}^2(\Omega_S) \times \mathbf{H}_{\Gamma_S}^2(\Omega_S) \rightarrow \mathbb{R}$, $b(\bullet, \bullet) : \mathbf{H}_{\Gamma_S}^2(\Omega_S) \times \mathbf{H}^1(\Omega_D) \rightarrow \mathbb{R}$, and $c(\bullet, \bullet) : \mathbf{H}^1(\Omega_D) \times \mathbf{H}^1(\Omega_D) \rightarrow \mathbb{R}$ together with the linear forms $\mathbf{F}(\bullet) : \mathbf{H}_{\Gamma_S}^2(\Omega_S) \rightarrow \mathbb{R}$ and $\mathbf{G}(\bullet) : \mathbf{H}^1(\Omega_D) \rightarrow \mathbb{R}$ given by

$$a(\chi, \xi) = \langle \mathbf{A}\chi, \xi \rangle := \mu \int_{\Omega_S} \nabla^2 \chi : \nabla^2 \xi + \frac{\alpha \mu}{\sqrt{\kappa}} \int_{\Sigma} (\nabla \chi \cdot \mathbf{n}_{\Sigma})(\nabla \xi \cdot \mathbf{n}_{\Sigma}) =: a^{\nabla^2}(\chi, \xi) + a^{\Sigma}(\chi, \xi),$$

$$b(\xi, \psi) = \langle \mathbf{B}\xi, \psi \rangle := \int_{\Sigma} \psi \nabla \xi \cdot \mathbf{t}_{\Sigma}, \quad c(\varphi, \psi) = \langle \mathbf{C}\varphi, \psi \rangle := \kappa \int_{\Omega_D} \nabla \varphi \cdot \nabla \psi,$$

$$\mathbf{F}(\xi) := \int_{\Omega_S} \mathbf{f} \cdot \mathbf{curl} \xi, \quad \mathbf{G}(\psi) := - \int_{\Omega_D} g \psi,$$

where $\mathbf{A} : \mathbf{H}_{\Gamma_S}^2(\Omega_S) \rightarrow [\mathbf{H}_{\Gamma_S}^2(\Omega_S)]'$, $\mathbf{B} : \mathbf{H}_{\Gamma_S}^2(\Omega_S) \rightarrow [\mathbf{H}^1(\Omega_D)]'$, and $\mathbf{C} : \mathbf{H}^1(\Omega_D) \rightarrow [\mathbf{H}^1(\Omega_D)]'$ are the linear operators induced by $a(\bullet, \bullet)$, $b(\bullet, \bullet)$, and $c(\bullet, \bullet)$, respectively. Note that $\mathbf{F} \in [\mathbf{H}_{\Gamma_S}^2(\Omega_S)]'$ and $\mathbf{G} \in [\mathbf{H}^1(\Omega_D)]'$, where the notation $[\mathbf{H}_{\Gamma_S}^2(\Omega_S)]'$ (resp. $[\mathbf{H}^1(\Omega_D)]'$) indicates the dual space of $\mathbf{H}_{\Gamma_S}^2(\Omega_S)$ (resp. $\mathbf{H}^1(\Omega_D)$). These definitions lead to the following perturbed saddle–point problem (equivalent to (8)) written in operator form, i.e., in the dual of the solution space, given by

$$\begin{pmatrix} \mathbf{A} & \mathbf{B}^* \\ \mathbf{B} & -\mathbf{C} \end{pmatrix} \begin{pmatrix} \chi \\ \varphi \end{pmatrix} = \begin{pmatrix} \mathbf{F} \\ \mathbf{G} \end{pmatrix}, \quad \text{in } [\mathbf{H}_{\Gamma_S}^2(\Omega_S) \times \mathbf{H}^1(\Omega_D)]'. \quad (9)$$

2.3 Well-posedness of the continuous problem

We now aim to prove the well-posedness of the problem provided in (9). First, we collect in the lemma below the properties of the linear operators involved in the formulation.

Lemma 1 (properties of the continuous operators) *The following bounds hold:*

$$|\langle \mathbf{A}\chi, \xi \rangle| \lesssim \mu \max \left\{ 1, \frac{\alpha}{\sqrt{\kappa}} \right\} \|\chi\|_{2, \Omega_S} \|\xi\|_{2, \Omega_S}, \quad \forall \chi, \xi \in \mathbf{H}_{\Gamma_S}^2(\Omega_S), \quad (10a)$$

$$\langle \mathbf{A}\xi, \xi \rangle \geq \mu \|\xi\|_{2, \Omega_S}^2, \quad \forall \xi \in \mathbf{H}_{\Gamma_S}^2(\Omega_S), \quad (10b)$$

$$|\langle \mathbf{B}\xi, \psi \rangle| \lesssim \|\xi\|_{2, \Omega_S} \|\psi\|_{1, \Omega_D}, \quad \forall \xi \in \mathbf{H}_{\Gamma_S}^2(\Omega_S), \forall \psi \in \mathbf{H}^1(\Omega_D), \quad (10c)$$

$$|\langle \mathbf{C}\varphi, \psi \rangle| \leq \kappa \|\varphi\|_{1, \Omega_D} \|\psi\|_{1, \Omega_D}, \quad \forall \varphi, \psi \in \mathbf{H}^1(\Omega_D), \quad (10d)$$

$$|\mathbf{F}(\xi)| \lesssim \|\mathbf{f}\|_{0, \Omega_S} \|\xi\|_{2, \Omega_S}, \quad \forall \xi \in \mathbf{H}_{\Gamma_S}^2(\Omega_S), \quad (10e)$$

$$|\mathbf{G}(\psi)| \lesssim \|g\|_{0, \Omega_D} \|\psi\|_{1, \Omega_D}, \quad \forall \psi \in \mathbf{H}^1(\Omega_D). \quad (10f)$$

Proof Standard arguments involving the Cauchy–Schwarz inequality, the trace inequality (used in (10a), (10c), and (10f)), and the Poincaré inequality (used in (10e) and (10f)), lead to the result. \square

Following [32], the kernel of the system (9) is characterised next.

Lemma 2 (kernel characterisation) *Let $(\chi, \varphi) \in \mathbf{H}_{\Gamma_S}^2(\Omega_S) \times \mathbf{H}^1(\Omega_D)$ be a solution to the homogeneous system in (9). Then, there exists $\lambda \in \mathbb{R}$ such that*

$$(\chi, \varphi) = (0, \lambda).$$

Proof Starting from (9), we can rewrite the problem in operator form as

$$\mathbf{A}\chi + \mathbf{C}\varphi = 0 \quad \text{in} \quad [\mathbf{H}_{\Gamma_S}^2(\Omega_S) \times \mathbf{H}^1(\Omega_D)]'.$$

Testing this equation with $(\chi, \varphi) \in \mathbf{H}_{\Gamma_S}^2(\Omega_S) \times \mathbf{H}^1(\Omega_D)$ and using the coercivity of \mathbf{A} (cf. (10b)) together with the definition of \mathbf{C} , we obtain

$$\mu \|\chi\|_{2, \Omega_S}^2 + \kappa |\varphi|_{1, \Omega_D}^2 \leq 0.$$

Therefore, we deduce that $\chi = 0$ and $\varphi = \lambda$ for some $\lambda \in \mathbb{R}$. □

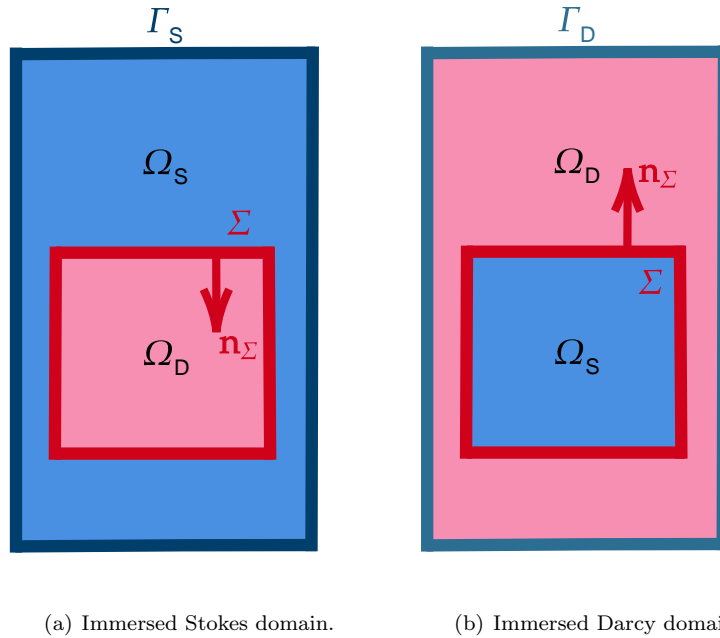


Fig. 2 Schematic representations of the two nested Stokes–Darcy domain configurations.

Remark 2.2 In addition to the domain setting discussed in Remark 2.1, we recall that two additional configurations can be taken into account:

1. A Darcy domain immersed in a Stokes domain. In this case, the simply connected assumption of the Stokes domain is not satisfied anymore (see Fig. 2(b)). Consequently, the stream function is not uniquely determined by the standard boundary conditions. Instead, $\chi = C_i \in \mathbb{R}$ on $\Gamma_i \subset \Sigma$, where Γ_i is the i -th connected component of Σ . As established in [34], the following compatibility condition must be satisfied at the continuous level

$$\oint_{\Sigma} \frac{\partial(\Delta\psi)}{\partial n} d\tau = 0. \quad (11)$$

Such requirement can be used to uniquely determine the values of C_i (see [41] for more details). The additional difficulties associated with the non-simply connected Stokes stream-function formulation do not affect the Darcy domain, and Lemma 2 remains valid.

2. A Stokes domain immersed in a Darcy domain. Alternatively, the inverse configuration is depicted in Fig. 2(a). Since no boundary conditions are defined for the stream functions, we require a different functional setting in order to recover the coercivity (cf. (10b)) of the operator \mathbf{A} . The space related to the stream function is defined by

$$\mathbf{H}_\star^2(\Omega_S) := \left\{ \xi \in \mathbf{H}^2(\Omega_S) \setminus \mathbb{R} : \int_{\Omega_S} \xi = 0, \int_{\Omega_S} \nabla \xi = \mathbf{0} \right\}, \quad (12)$$

which together with $\alpha > 0$ and the Poincaré inequality establish the required coercivity.

Observe that Lemma 2 naturally motivates the introduction of the Hilbertian space

$$\mathbf{H}_\star^1(\Omega_D) := \left\{ \psi \in \mathbf{H}^1(\Omega_D) : \int_{\Omega_D} \psi = 0 \right\},$$

which ensures the uniqueness of the Darcy pressure φ in the kernel of the operator on the left-hand side of equation (9), in particular, it enforces $\lambda = 0$ in Lemma 2. For this reason, in what follows we seek $\varphi \in \mathbf{H}_\star^1(\Omega_D)$. Notice that this additional constraint allows us to deduce the equivalence between $\|\bullet\|_{1,\Omega_D}$ and $|\bullet|_{1,\Omega_D}$ on $\mathbf{H}_\star^1(\Omega_D)$ owing to the Poincaré inequality. Consequently, this property leads to the coercivity of the operator C , that is,

$$\langle \mathbf{C}\psi, \psi \rangle \gtrsim \kappa \|\psi\|_{1,\Omega_D}^2, \quad \forall \psi \in \mathbf{H}_\star^1(\Omega_D). \quad (13)$$

Remark 2.3 In light of Remark 2.1, we readily see that the natural Hilbert space associated to the Darcy pressure φ (in both the full Dirichlet and mixed boundary conditions settings) is given by

$$\mathbf{H}_{\Gamma_D}^1(\Omega_D) := \{\psi \in \mathbf{H}^1(\Omega_D) : \psi = 0 \text{ on } \Gamma_D\}.$$

This observation yields an analogue of the coercivity result for the operator \mathbf{C} (cf. (13)) in this space. On the other hand, following Remark 2.2, we note that (6a) calls for a different functional setting for the stream function to recover the coercivity of the operator \mathbf{A} (see (10b)). The appropriate choice is the space defined in (12).

Let us define the global operator $\mathcal{A} : (\mathbf{H}_{\Gamma_S}^2(\Omega_S) \times \mathbf{H}_\star^1(\Omega_D)) \times (\mathbf{H}_{\Gamma_S}^2(\Omega_S) \times \mathbf{H}_\star^1(\Omega_D)) \rightarrow \mathbb{R}$ as

$$\mathcal{A}((\chi, \varphi), (\xi, \psi)) := a(\chi, \xi) + b(\xi, \varphi) + b(\chi, \psi) - c(\varphi, \psi),$$

together with the graph norm in the space $\mathbf{H}_{\Gamma_S}^2(\Omega_S) \times \mathbf{H}_\star^1(\Omega_D)$ defined by $\|(\xi, \psi)\|^2 := \|\xi\|_{2,\Omega_S}^2 + \|\psi\|_{1,\Omega_D}^2$. We readily see that the boundedness of \mathcal{A} is provided by Lemma 1. The global inf-sup condition for the operator \mathcal{A} is provided below.

Lemma 3 (global inf-sup condition) *The following bound holds:*

$$\sup_{(\xi, \psi) \in (\mathbf{H}_{\Gamma_S}^2(\Omega_S) \times \mathbf{H}_\star^1(\Omega_D)) \setminus \{(0,0)\}} \frac{\mathcal{A}((\chi, \varphi), (\xi, \psi))}{\|(\xi, \psi)\|} \gtrsim \|(\chi, \varphi)\|, \quad \forall (\chi, \varphi) \in \mathbf{H}_{\Gamma_S}^2((\Omega_S) \times \mathbf{H}_\star^1(\Omega_D)).$$

Proof The proof follows by testing with $(\xi, \psi) = (\chi, -\varphi)$. Indeed, using the coercivity of the operators \mathbf{A} and \mathbf{C} (cf. (10b) and (13)), we obtain the desired estimate. The details are standard and therefore omitted. \square

Finally, the well-posedness of the perturbed saddle–point problem and the continuous dependence on data follows from the global inf-sup above combined with a direct application of the Babuška–Brezzi theory.

Theorem 1 (continuous well-posedness) *There exists a unique solution $(\chi, \varphi) \in \mathbf{H}_{\Gamma_S}^2(\Omega_S) \times \mathbf{H}_\star^1(\Omega_D)$ to (9) (equivalently, (8)) such that*

$$\|(\chi, \varphi)\| \lesssim \|\mathbf{f}\|_{0,\Omega_S} + \|g\|_{0,\Omega_D}.$$

3 Virtual element discretisation

This section introduces the conforming lowest-order virtual element discretisation, i.e., quadratic C^1 -VEM for stream functions χ and linear C^0 -VEM for pressure φ . In addition, we define the associated polynomial projection operators and provide the corresponding approximation and interpolation estimates. Finally, we introduce the discrete version of (8).

Admissible meshes and scaled monomials. Let \mathcal{T}_h be a collection of polygonal meshes on $\Omega_S \cup \Omega_D$ and \mathcal{E}_h be the set of all edges. The diameter of a polygon $K \in \mathcal{T}_h$ (resp. edge $e \in \mathcal{E}_h$) is denoted by h_K (resp. h_e). The maximum diameter of elements in \mathcal{T}_h is represented by h . It is assumed that there exists a constant $\eta > 0$ such that

- (M1) every polygon K is star-shaped with respect to a ball of a radius greater than ηh_K ,
- (M2) every edge $e \in \partial K$ satisfies the inequality $h_e \geq \eta h_K$.

In view of the boundary conditions, we denote by \mathbf{t}_e and \mathbf{n}_e the unit tangential and normal vector of e with respect to ∂K ; we simply write \mathbf{t} and \mathbf{n} when the context is sufficiently clear. The polygonal mesh associated to Ω_S (resp. Ω_D) is defined by $\mathcal{T}_h(\Omega_S) := \{K \in \mathcal{T}_h : K \subset \Omega_S\}$ (resp. $\mathcal{T}_h(\Omega_D) := \{K \in \mathcal{T}_h : K \subset \Omega_D\}$), while the set of edges lying in the interface Σ is given by $\mathcal{E}_h(\Sigma) := \{e \in \mathcal{E}_h : e \subset \Sigma\}$ and $\mathcal{T}_h(\Omega_S) \cap \mathcal{T}_h(\Omega_D) = \mathcal{E}_h(\Sigma)$.

Let $K \in \mathcal{T}_h$ be a polygon with barycenter $\mathbf{x}_K := (x_{1,K}, x_{2,K})^\dagger$, and $M_k(K)$ for $k \geq 0$ be the set of scalar scaled monomials defined by

$$M_k(K) := \left\{ \left(\frac{\mathbf{x} - \mathbf{x}_P}{h_P} \right)^\alpha, 0 \leq |\alpha| \leq k \right\},$$

where $\alpha = (\alpha_1, \alpha_2)^\dagger$ is a non-negative multi-index such that $\mathbf{x}^\alpha := x_1^{\alpha_1} x_2^{\alpha_2}$ with $\mathbf{x} = (x_1, x_2)^\dagger$ and $|\alpha| = \alpha_1 + \alpha_2$. Note that $M_k(K)$ defines a basis for the space of scalar polynomials of degree at most k , denoted by $P_k(K)$.

3.1 Polynomial projection operators

For each polygon $K \in \mathcal{T}_h$, we introduce the following local polynomial projection operators:

1. The L^2 -projection $\Pi_1^{0,K} : L^2(K) \rightarrow P_1(K)$ is defined, for any $\phi \in L^2(K)$, by

$$\int_K (\Pi_1^{0,K} \phi - \phi) m_1 = 0, \quad \forall m_1 \in M_1(K). \quad (14)$$

2. The H^1 -projection $\Pi_1^{\nabla,K} : H^1(K) \rightarrow P_1(K)$ is defined, for any $\phi \in H^1(K)$, by

$$\int_K \nabla(\Pi_1^{\nabla,K} \phi - \phi) \cdot \nabla m_1 = 0, \quad \forall m_1 \in M_1(K), \quad (15a)$$

$$\int_{\partial K} \Pi_1^{\nabla,K} \phi - \phi = 0. \quad (15b)$$

3. The H^2 -projection $\Pi_2^{\nabla^2,K} : H^2(K) \rightarrow P_2(K)$ is defined, for any $\phi \in H^2(K)$, by

$$\int_K \nabla^2(\Pi_2^{\nabla^2,K} \phi - \phi) : \nabla^2 m_2 = 0, \quad \forall m_2 \in M_2(K), \quad (16a)$$

$$\int_{\partial K} \Pi_2^{\nabla^2,K} \phi - \phi = 0, \quad (16b)$$

$$\int_{\partial K} \nabla(\Pi_2^{\nabla^2,K} \phi - \phi) = 0. \quad (16c)$$

We finalise this section by recalling a classical result from polynomial approximation theory [14].

Lemma 4 (polynomial projection estimates) *For any $K \in \mathcal{T}_h$, suppose that $\phi \in H^s(K)$ and $\phi_\pi \in P_{k+1}(K)$, with $0 \leq s \leq k+1$. Then, there exists a positive constant that depends only on η (cf. (M1)-(M2)) such that, for $0 \leq r \leq s$ the following estimate holds*

$$|\phi - \phi_\pi|_{r,K} \lesssim h_K^{s-r} |\phi|_{s,K}.$$

Remark 3.1 In practice, the polynomial approximation ϕ_π of $\phi \in H^s(K)$ corresponds to the polynomial projections $\Pi_1^{0,K} \phi$, $\Pi_1^{\nabla,K} \phi$, or $\Pi_2^{\nabla^2,K} \phi$ for $s \geq 0, 1$, or 2 , respectively.

3.2 C^1 -VEM space

To approximate the functional space associated to the stream functions we consider the following local enhanced virtual space for any $K \in \mathcal{T}_h(\Omega_S)$ given by

$$\begin{aligned} \Xi_h(K) := & \left\{ \xi_h \in H^2(K) : \Delta^2 \xi_h \in P_2(K), \right. \\ & \xi_h|_{\partial K} \in C^0(\partial K), \xi_h|_e \in P_3(e), \forall e \in \partial K, \\ & \nabla \xi_h|_{\partial K} \in [C^0(\partial K)]^2, (\nabla \xi_h \cdot \mathbf{n}_e)|_e \in P_1(e), \forall e \in \partial K, \\ & \left. \int_K (\Pi_2^{\nabla^2} \xi_h - \xi_h) m_2 = 0, \forall m_2 \in M_2(K) \right\}. \end{aligned}$$

We select the unisolvent set of DoFs for $\Xi_h(K)$ as follows:

- (D1) $_{\xi_h}$) the values of ξ_h at the vertices of K ,
- (D2) $_{\xi_h}$) the values of $h_{V_i} \nabla \xi_h$ at the vertices of K ,

where h_{V_i} corresponds to the average of diameters h_K corresponding to the elements K that have V_i as a vertex. Thanks to the enhancement condition, the projection operators $\Pi_2^{\nabla^2,K}$ and $\Pi_2^{0,K}$ coincide (see [47]). Furthermore, they can be directly computed from the DoFs provided above. We refer to [4] for further details regarding unisolvence and computability. The global virtual space for stream functions is defined as follows

$$\Xi_h := \{ \xi_h \in H_{\Gamma_S}^2(\Omega_S) : \xi_h|_K \in \Xi_h(K), \forall K \in \mathcal{T}_h(\Omega_S) \}.$$

Note that the space Ξ_h has $3N_S$ DoFs, where N_S is the total number of interior vertices of the polygonal mesh $\mathcal{T}_h(\Omega_S)$. Moreover, notice that the patching of local spaces across the mesh skeleton ensures global C^1 -conformity, as the shared degrees of freedom uniquely determine both the function and its normal derivative along element interfaces.

3.3 C^0 -VEM space

To approximate the Darcy pressure space, for any $K \in \mathcal{T}_h(\Omega_D)$ we consider the local enhanced virtual space given by

$$\begin{aligned} \Psi_h(K) := & \left\{ \psi_h \in H^1(K) : \Delta \psi_h \in P_1(K), \right. \\ & \psi_h|_e \in C^0(\partial K), \psi_h|_e \in P_1(e), \forall e \in \partial K, \\ & \left. \int_K (\Pi_1^{\nabla,K} \psi_h - \psi_h) m_1 = 0, \forall m_1 \in M_1(K) \right\}, \end{aligned}$$

equipped with the following unisolvent set of DoFs:

- (D1) $_{\psi_h}$) The values of ψ_h at the vertices of K .

We recall that the projection operators $\Pi_1^{\nabla,K}$ and $\Pi_1^{0,K}$ coincide on $\Psi_h(K)$ and are computable via the previously defined DoFs. Additionally, the unisolvence of the space is established in [8,9]. Similarly, the global VEM pressure space is defined by

$$\Psi_h := \{ \psi_h \in \mathbf{H}_*^1(\Omega_D) : \psi_h|_K \in \Psi_h(K), \forall K \in \mathcal{T}_h(\Omega_D) \}.$$

For this space, there are N_D total number of DoFs for the space Ψ_h , with N_D denoting the number of interior vertices of the polygonal mesh $\mathcal{T}_h(\Omega_D)$. In addition, the global space Ξ_h is constructed by gluing the local spaces $\Xi_h(K)$ across the mesh skeleton, where the matching of vertex values guarantees C^0 -continuity across element interfaces. Finally, at the implementation level, the zero mean condition of the space $\mathbf{H}_*^1(\Omega_D)$ is imposed through a scalar Lagrange multiplier.

3.4 Discrete formulation and unique solvability

First, we define the discrete bilinear forms $a_h(\bullet, \bullet) : \Xi_h \times \Xi_h \rightarrow \mathbb{R}$, $b(\bullet, \bullet) : \Xi_h \times \Psi_h \rightarrow \mathbb{R}$, $c_h(\bullet, \bullet) : \Psi_h \times \Psi_h \rightarrow \mathbb{R}$, and the linear forms $F_h(\bullet) : \Xi_h \rightarrow \mathbb{R}$, $G_h(\bullet) : \Psi_h \rightarrow \mathbb{R}$ locally as

$$\begin{aligned} a_h(\chi_h, \xi_h) &= \langle \mathbf{A}_h \chi_h, \xi_h \rangle = \sum_{K \in \mathcal{T}_h(\Omega_S)} a_h^K(\chi_h, \xi_h) = \sum_{K \in \mathcal{T}_h(\Omega_S)} \left[a_h^{\nabla^2,K}(\chi_h, \xi_h) + a_h^{\Sigma,K}(\chi_h, \xi_h) \right] \\ &:= \sum_{K \in \mathcal{T}_h(\Omega_S)} \left[\mu \int_K \nabla^2(\Pi_2^{\nabla^2,K} \chi_h) : (\nabla^2 \Pi_2^{\nabla^2,K} \xi_h) + S_S^K(\chi_h - \Pi_2^{\nabla^2,K} \chi_h, \xi_h - \Pi_2^{\nabla^2,K} \xi_h) \right. \\ &\quad \left. + \sum_{e \in \mathcal{E}_h(\Sigma) \cap \partial K} \frac{\alpha \mu}{\sqrt{\kappa}} \int_e (\nabla \chi_h \cdot \mathbf{n}_\Sigma)(\nabla \xi_h \cdot \mathbf{n}_\Sigma) \right], \\ b(\xi_h, \psi_h) &= \langle \mathbf{B} \xi_h, \psi_h \rangle = \sum_{K \in \mathcal{T}_h} b^K(\xi_h, \psi_h) \\ &:= \sum_{K \in \mathcal{T}_h} \sum_{e \in \mathcal{E}_h(\Sigma) \cap \partial K} \frac{1}{2} \int_e \psi_h \nabla \xi_h \cdot \mathbf{t}_\Sigma = \sum_{e \in \mathcal{E}_h(\Sigma)} \int_e \psi_h \nabla \xi_h \cdot \mathbf{t}_\Sigma, \\ c_h(\varphi_h, \psi_h) &= \langle \mathbf{C}_h \varphi_h, \psi_h \rangle = \sum_{K \in \mathcal{T}_h(\Omega_D)} c_h^K(\varphi_h, \psi_h) \\ &:= \sum_{K \in \mathcal{T}_h(\Omega_D)} \kappa \int_K \nabla(\Pi_1^{\nabla,K} \varphi_h) \cdot \nabla(\Pi_1^{\nabla,K} \psi_h) + S_D^K(\varphi_h - \Pi_1^{\nabla,K} \varphi_h, \psi_h - \Pi_1^{\nabla,K} \psi_h), \\ F_h(\xi_h) &= \sum_{K \in \mathcal{T}_h(\Omega_S)} F_h^K(\xi_h) := \sum_{K \in \mathcal{T}_h(\Omega_S)} \int_K \mathbf{f} \cdot \mathbf{curl}(\Pi_2^{\nabla^2,K} \xi_h), \\ G_h(\psi_h) &= \sum_{K \in \mathcal{T}_h(\Omega_D)} G_h^K(\psi_h) := - \sum_{K \in \mathcal{T}_h(\Omega_D)} \int_K g \Pi_1^{0,K} \psi_h, \end{aligned}$$

where $\mathbf{A}_h : \Xi_h \rightarrow (\Xi_h)'$ (resp. $\mathbf{C}_h : \Psi_h \rightarrow (\Psi_h)'$) is the linear operator induced by $a_h(\bullet, \bullet)$ (resp. $c_h(\bullet, \bullet)$), the superscript K indicates the restriction to the polygon K , and the stabilisation operators $S_S^K : \Xi_h(K) \times \Xi_h(K) \rightarrow \mathbb{R}$ and $S_D^K : \Psi_h(K) \times \Psi_h(K) \rightarrow \mathbb{R}$ are any positive semi-definite inner products satisfying

$$a^{\nabla^2,K}(\xi_h, \xi_h) \lesssim S_S^K(\xi_h, \xi_h) \lesssim a^{\nabla^2,K}(\xi_h, \xi_h), \quad \forall \xi_h \in \ker(\Pi_2^{\nabla^2,K}), \quad (17a)$$

$$c^K(\psi_h, \psi_h) \lesssim S_D^K(\psi_h, \psi_h) \lesssim c^K(\psi_h, \psi_h), \quad \forall \psi_h \in \ker(\Pi_1^{\nabla,K}). \quad (17b)$$

Next, we introduce the discrete version of the stream function – pressure weak formulation for the Stokes–Darcy interface problem (cf. (8)) as follows: given $\mathbf{f} \in \mathbf{L}^2(\Omega_S)$ and $g \in L_0^2(\Omega_D)$, find $(\chi_h, \varphi_h) \in \Xi_h \times \Psi_h$ such that

$$a_h(\chi_h, \xi_h) + b(\xi_h, \varphi_h) = F_h(\xi_h), \quad \forall \xi_h \in \Xi_h, \quad (18a)$$

$$b(\chi_h, \psi_h) - c_h(\varphi_h, \psi_h) = G_h(\psi_h), \quad \forall \psi_h \in \Psi_h. \quad (18b)$$

Similarly, the respective perturbed saddle-point (in operator form) equivalent to (18) reads

$$\begin{pmatrix} \mathbf{A}_h & \mathbf{B}^* \\ \mathbf{B} & -\mathbf{C}_h \end{pmatrix} \begin{pmatrix} \chi_h \\ \varphi_h \end{pmatrix} = \begin{pmatrix} F_h \\ G_h \end{pmatrix}, \quad \text{in } [\Xi_h \times \Psi_h]'. \quad (19)$$

The properties of the discrete linear operators are provided in the following lemma, recalling that the relation $\|\bullet\|_{s,\Omega_\square}^2 = \sum_{K \in \mathcal{T}_h(\Omega_\square)} \|\bullet\|_{s,K}^2$ holds for $s \in \{0, 1, 2\}$ and $\square \in \{S, D\}$.

Lemma 5 (properties of the discrete operators) *The following bounds hold*

$$|\langle \mathbf{A}_h \chi_h, \xi_h \rangle| \lesssim \mu \max \left\{ 1, \frac{\alpha}{\sqrt{\kappa}} \right\} \|\chi_h\|_{2,\Omega_S} \|\xi_h\|_{2,\Omega_S}, \quad \forall \chi_h, \xi_h \in \Xi_h, \quad (20a)$$

$$\langle \mathbf{A}_h \xi_h, \xi_h \rangle \gtrsim \mu \|\xi_h\|_{2,\Omega_S}^2, \quad \forall \xi_h \in \Xi_h, \quad (20b)$$

$$|\langle \mathbf{C}_h \varphi_h, \psi_h \rangle| \lesssim \kappa \|\varphi_h\|_{1,\Omega_D} \|\psi_h\|_{1,\Omega_D}, \quad \forall \varphi_h, \psi_h \in \Psi_h, \quad (20c)$$

$$\langle \mathbf{C}_h \psi_h, \psi_h \rangle \gtrsim \kappa \|\psi_h\|_{1,\Omega_D}^2, \quad \forall \psi_h \in \Psi_h, \quad (20d)$$

$$|\mathbf{F}_h(\xi_h)| \lesssim \|\mathbf{f}\|_{0,\Omega_S} \|\xi_h\|_{2,\Omega_S}, \quad \forall \xi_h \in \Xi_h, \quad (20e)$$

$$|\mathbf{G}_h(\psi_h)| \lesssim \|g\|_{0,\Omega_D} \|\psi_h\|_{1,\Omega_D}, \quad \forall \psi_h \in \Psi_h. \quad (20f)$$

Proof Standard arguments (cf. Lemma 1) together with the stabilisation bounds (17) lead to the result, further details are omitted. \square

We now define the discrete global operator $\mathcal{A}_h : (\Xi_h \times \Psi_h) \times (\Xi_h \times \Psi_h) \rightarrow \mathbb{R}$ as

$$\mathcal{A}_h((\chi_h, \varphi_h), (\xi_h, \psi_h)) := a_h(\chi_h, \xi_h) + b(\xi_h, \varphi_h) + b(\chi_h, \psi_h) - c_h(\varphi_h, \psi_h),$$

and the graph norm in the space $\Xi_h \times \Psi_h$ is defined by $\|(\xi_h, \psi_h)\|^2 := \|\xi_h\|_{2,\Omega_S}^2 + \|\psi_h\|_{1,\Omega_D}^2$. Similarly, the boundedness of \mathcal{A}_h is provided by Lemma 5. Now, the discrete global inf-sup condition for the operator \mathcal{A}_h is provided below as a consequence of (20b) and (20d) (see also Theorem 3).

Lemma 6 (discrete global inf-sup) *The following bound holds:*

$$\sup_{(\chi_h, \varphi_h) \in (\Xi_h \times \Psi_h) \setminus \{(0,0)\}} \frac{\mathcal{A}_h((\chi_h, \varphi_h), (\xi_h, \psi_h))}{\|(\xi_h, \psi_h)\|} \gtrsim \|(\chi_h, \varphi_h)\|, \quad \forall (\chi_h, \varphi_h) \in \Xi_h \times \Psi_h.$$

The well-posedness of the discrete perturbed saddle–point problem (cf. (19)) and the discrete continuous dependence on data is stated below.

Theorem 2 (discrete well-posedness) *There exists a unique solution $(\chi_h, \varphi_h) \in \Xi_h \times \Psi_h$ to (19) (equivalently, (18)) such that*

$$\|(\chi_h, \varphi_h)\| \lesssim \|\mathbf{f}\|_{0,\Omega_S} + \|g\|_{0,\Omega_D}.$$

Note that the hidden constant in Theorem 2 may differ from that in Theorem 1.

4 A priori error analysis

This section is devoted to the derivation of an a priori error estimate for the VEM discretisation discussed in Section 3. We start by recalling the interpolation properties of the spaces Ξ_h and Ψ_h (see e.g. [4, 20, 38, 46, 8]).

Lemma 7 (interpolation estimates) *Let $\xi \in \mathbf{H}_{T_S}^2(\Omega_S) \cap \mathbf{H}^{r_1}(\Omega_S)$ and $\psi \in \mathbf{H}_*^1(\Omega_D) \cap \mathbf{H}^{r_2}(\Omega_D)$ with $2 \leq r_1 \leq 3$ and $1 \leq r_2 \leq 2$. Then, there exist interpolation operators $\mathbf{I}_{S,h} : \mathbf{H}_{T_S}^2(\Omega_S) \cap \mathbf{H}^{r_1}(\Omega_S) \rightarrow \Xi_h$ and $\mathbf{I}_{D,h} : \mathbf{H}_*^1(\Omega_D) \cap \mathbf{H}^{r_2}(\Omega_D) \rightarrow \Psi_h$, such that*

$$\begin{aligned} |\xi - \mathbf{I}_{S,h}^K \xi|_{j_1, K_S} &\lesssim h_K^{r_1 - j_1} |\xi|_{r_1, K_S}, \quad 0 \leq j_1 \leq 2, \quad \forall K_S \in \mathcal{T}_h(\Omega_S), \\ |\psi - \mathbf{I}_{D,h}^K \psi|_{j_2, K_D} &\lesssim h_K^{r_2 - j_2} |\psi|_{r_2, K_D}, \quad 0 \leq j_2 \leq 1, \quad \forall K_D \in \mathcal{T}_h(\Omega_D), \end{aligned}$$

where $\mathbf{I}_{\square,h}^K$ denotes the restriction of the global interpolant $\mathbf{I}_{\square,h}$ to the local element K_\square for both the solid and fluid subdomains, i.e., $\square \in \{S, D\}$.

We now define the total error as

$$e_h := \|(\chi - \chi_h, \varphi - \varphi_h)\| = (e_{\chi_h}^2 + e_{\varphi_h}^2)^{\frac{1}{2}},$$

where $e_{\chi_h} := \|\chi - \chi_h\|_{2,\Omega_S}$ and $e_{\varphi_h} := \|\varphi - \varphi_h\|_{1,\Omega_D}$. The following result provides a bound of e_h in terms of the data approximation, polynomial approximation, and interpolation errors.

Lemma 8 (energy-error estimate) *Let $(\chi, \varphi) \in \mathbf{H}_{\Gamma_S}^2(\Omega_S) \times \mathbf{H}_*^1(\Omega_D)$ and $(\chi_h, \varphi_h) \in \Xi_h \times \Psi_h$ be the unique solutions to (9) and (19), respectively. Then, the following estimate holds:*

$$e_h \lesssim \max \left\{ 1, \mu, \kappa, \frac{\mu\alpha}{\sqrt{\kappa}} \right\} \left(\sum_{K \in \mathcal{T}_h(\Omega_S)} \left[|\chi - \mathbf{I}_{S,h}^K \chi|_{2,K} + |\chi - \Pi_2^{\nabla^2,K} \chi|_{2,K} + \|F^K - F_h^K\|_{(\Xi_h(K))'} \right] \right. \\ \left. + \sum_{K \in \mathcal{T}_h(\Omega_D)} \left[|\varphi - \mathbf{I}_{D,h}^K \varphi|_{1,K} + |\varphi - \Pi_1^{\nabla,K} \varphi|_{1,K} + \|G^K - G_h^K\|_{(\Psi_h(K))'} \right] \right).$$

Proof From the unique solvability of both continuous weak formulation (8) and the discrete weak formulation (18) we readily see that $(\chi_h - \mathbf{I}_{S,h} \chi, \varphi_h - \mathbf{I}_{D,h} \varphi) \in \Xi_h \times \Psi_h$ is the unique solution to

$$a_h(\chi_h - \mathbf{I}_{S,h} \chi, \xi_h) + b(\xi_h, \varphi_h - \mathbf{I}_{D,h} \varphi) = \check{F}_h(\xi_h), \quad \forall \xi_h \in \Xi_h, \\ b(\chi_h - \mathbf{I}_{S,h} \chi, \psi_h) - c_h(\varphi_h - \mathbf{I}_{D,h} \varphi, \psi_h) = \check{G}_h(\psi_h), \quad \forall \psi_h \in \Psi_h,$$

where the right-hand sides are given by

$$\check{F}_h(\xi_h) := [a(\chi, \xi_h) - a_h(\mathbf{I}_{S,h} \chi, \xi_h)] + b(\xi_h, \varphi - \mathbf{I}_{D,h} \varphi) + [F_h - F](\xi_h), \quad (21a)$$

$$\check{G}_h(\psi_h) := [c_h(\mathbf{I}_{D,h} \varphi, \psi_h) - c(\varphi, \psi_h)] + b(\chi - \mathbf{I}_{S,h} \chi, \psi_h) + [G_h - G](\psi_h). \quad (21b)$$

The continuous dependence on data for the discrete problem (cf. Theorem 2) implies that

$$\|(\chi_h - \mathbf{I}_{S,h} \chi, \varphi_h - \mathbf{I}_{D,h} \varphi)\| \lesssim \|\check{F}_h\|_{\Xi_h'} + \|\check{G}_h\|_{\Psi_h'}.$$

We now focus in bounding the functionals appearing in (21). First, we recall the polynomial consistency of the discrete bilinear forms $a_h^{\nabla^2}(\bullet, \bullet)$ and $c_h(\bullet, \bullet)$, i.e.,

$$a_h^{\nabla^2,K}(\Pi_2^{\nabla^2,K} \chi_h, \xi_h) = a^{\nabla^2,K}(\Pi_2^{\nabla^2,K} \chi_h, \xi_h), \quad \forall \xi_h \in \Xi_h, \\ c_h^K(\Pi_1^{\nabla,K} \varphi_h, \psi_h) = c^K(\Pi_1^{\nabla,K} \varphi_h, \psi_h), \quad \forall \psi_h \in \Psi_h.$$

Thus, (21) turns into

$$\check{F}_h(\xi_h) = \sum_{K \in \mathcal{T}_h(\Omega_S)} \left[a^{\nabla^2,K}(\chi - \Pi_2^{\nabla^2,K} \chi_h, \xi_h) - a_h^{\nabla^2,K}(\mathbf{I}_{S,h}^K \chi - \Pi_2^{\nabla^2,K} \chi_h, \xi_h) \right] \\ + \sum_{K \in \mathcal{T}_h(\Omega_S)} a^{\Sigma,K}(\chi - \mathbf{I}_{S,h}^K \chi, \xi_h) + \sum_{K \in \mathcal{T}_h} b^K(\xi_h, \varphi - \mathbf{I}_{D,h}^K \varphi) + \sum_{K \in \mathcal{T}_h(\Omega_S)} [F_h^K - F^K](\xi_h), \\ \check{G}_h(\psi_h) = \sum_{K \in \mathcal{T}_h(\Omega_D)} \left[c_h^K(\mathbf{I}_{D,h}^K \varphi - \Pi_1^{\nabla,K} \varphi_h, \psi_h) - c^K(\varphi - \Pi_1^{\nabla,K} \varphi_h, \psi_h) \right] \\ + \sum_{K \in \mathcal{T}_h} b^K(\chi - \mathbf{I}_{S,h}^K \chi, \psi_h) + \sum_{K \in \mathcal{T}_h(\Omega_D)} [G_h^K - G^K](\psi_h).$$

The triangle inequality, the Cauchy–Schwarz inequality, and the stabilisation properties in (17) yield

$$|\check{F}_h(\xi_h)| \lesssim \max \left\{ 1, \mu, \frac{\mu\alpha}{\sqrt{\kappa}} \right\} \left(\sum_{K \in \mathcal{T}_h(\Omega_S)} \left[(|\chi - \Pi_2^{\nabla^2,K} \chi_h|_{2,K} + \|\mathbf{I}_{S,h}^K \chi - \Pi_2^{\nabla^2,K} \chi_h\|_{2,K}) \|\xi_h\|_{2,K} \right] \right. \\ \left. + \sum_{e \in \mathcal{E}_h(\Sigma)} \|\nabla(\chi - \mathbf{I}_{S,h}^K \chi) \cdot \mathbf{n}_\Sigma\|_{0,e} \|\nabla \xi_h \cdot \mathbf{n}_\Sigma\|_{0,e} + \sum_{e \in \mathcal{E}_h(\Sigma)} \|\nabla \xi_h \cdot \mathbf{n}_\Sigma\|_{0,e} \|\varphi - \mathbf{I}_{D,h} \varphi\|_{0,e} \right. \\ \left. + \sum_{K \in \mathcal{T}_h(\Omega_S)} [F_h^K - F^K](\xi_h) \right), \\ |\check{G}_h(\psi_h)| \lesssim \max \{ 1, \kappa \} \left(\sum_{K \in \mathcal{T}_h(\Omega_D)} \left[(\|\mathbf{I}_{D,h}^K \varphi - \Pi_1^{\nabla,K} \varphi_h\|_{1,K} + \|\varphi - \Pi_1^{\nabla,K} \varphi_h\|_{1,K}) \|\psi_h\|_{1,K} \right] \right. \\ \left. + \sum_{e \in \mathcal{E}_h(\Sigma)} \|\nabla(\chi - \mathbf{I}_{S,h}^K \chi) \cdot \mathbf{n}_\Sigma\|_{0,e} \|\psi_h\|_{0,e} + \sum_{K \in \mathcal{T}_h(\Omega_D)} [G_h^K - G^K](\psi_h) \right).$$

Next, we apply the discrete trace inequality and the inverse estimates in [36, Lemma 3.5] and [23, Theorem 3.6] to obtain

$$\|\nabla \xi_h \cdot \mathbf{n}\|_{0,e} \lesssim h_K^{-\frac{1}{2}} |\xi_h|_{1,K} \quad \text{and} \quad \|\psi_h\|_{0,e} \lesssim h_K^{-\frac{1}{2}} \|\psi_h\|_{0,K}.$$

This, the triangle inequality and the inequality $\sum_i a_i b_i \leq (\sum_i a_i)(\sum_i b_i)$ (for any finite nonnegative sequences $(a_i)_i$ and $(b_i)_i$) lead to

$$\begin{aligned} |\check{\mathbb{F}}_h(\xi_h)| &\lesssim \max \left\{ 1, \mu, \frac{\mu\alpha}{\sqrt{\kappa}} \right\} \left(\left(\sum_{K \in \mathcal{T}_h(\Omega_S)} [|\chi - \mathbf{I}_{S,h}^K \chi|_{2,K} + |\chi - \Pi_2^{\nabla^2, K} \chi_h|_{2,K}] \right) \|\xi_h\|_{2,\Omega_S} \right. \\ &\quad + \left(\sum_{e \in \mathcal{E}_h(\Sigma)} h_K^{-\frac{1}{2}} \|\nabla(\chi - \mathbf{I}_{S,h}^K \chi) \cdot \mathbf{n}_\Sigma\|_{0,e} \right) \|\xi_h\|_{2,\Omega_S} \\ &\quad \left. + \left(\sum_{e \in \mathcal{E}_h(\Sigma)} h_K^{-\frac{1}{2}} \|\varphi - \mathbf{I}_{D,h}^K \varphi\|_{0,e} \right) \|\xi_h\|_{2,\Omega_S} + \sum_{K \in \mathcal{T}_h(\Omega_S)} [F_h^K - F^K](\xi_h) \right), \\ |\check{\mathbb{G}}_h(\psi_h)| &\lesssim \max \{1, \kappa\} \left(\left(\sum_{K \in \mathcal{T}_h(\Omega_D)} [|\varphi - \mathbf{I}_{D,h}^K \varphi|_{1,K} + |\varphi - \Pi_1^{\nabla, K} \varphi_h|_{1,K}] \right) \|\psi_h\|_{1,\Omega_D} \right. \\ &\quad \left. + \left(\sum_{e \in \mathcal{E}_h(\Sigma)} h_K^{-\frac{1}{2}} \|\nabla(\chi - \mathbf{I}_{S,h}^K \chi) \cdot \mathbf{n}_\Sigma\|_{0,e} \right) \|\psi_h\|_{1,\Omega_D} + \sum_{K \in \mathcal{T}_h(\Omega_D)} [G_h^K - G^K](\psi_h) \right). \end{aligned}$$

We now apply the supremum over all $\xi_h \in \Xi_h$ (resp. $\psi_h \in \Psi_h$) to arrive at

$$\begin{aligned} \|\check{\mathbb{F}}_h(\xi_h)\|_{\Xi'_h} &\lesssim \max \left\{ 1, \mu, \frac{\mu\alpha}{\sqrt{\kappa}} \right\} \left(\sum_{K \in \mathcal{T}_h(\Omega_S)} [|\chi - \mathbf{I}_{S,h}^K \chi|_{2,K} + |\chi - \Pi_2^{\nabla^2, K} \chi_h|_{2,K}] \right. \\ &\quad + \sum_{e \in \mathcal{E}_h(\Sigma)} h_K^{-\frac{1}{2}} \|\nabla(\chi - \mathbf{I}_{S,h}^K \chi) \cdot \mathbf{n}_\Sigma\|_{0,e} + \sum_{e \in \mathcal{E}_h(\Sigma)} h_K^{-\frac{1}{2}} \|\varphi - \mathbf{I}_{D,h}^K \varphi\|_{0,e} \\ &\quad \left. + \sum_{K \in \mathcal{T}_h(\Omega_S)} \|F_h^K - F^K\|_{(\Xi_h(K))'} \right), \\ \|\check{\mathbb{G}}_h(\psi_h)\|_{\Psi'_h} &\lesssim \max \{1, \kappa\} \left(\sum_{K \in \mathcal{T}_h(\Omega_D)} [|\varphi - \mathbf{I}_{D,h}^K \varphi|_{1,K} + |\varphi - \Pi_1^{\nabla, K} \varphi_h|_{1,K}] \right. \\ &\quad \left. + \sum_{e \in \mathcal{E}_h(\Sigma)} h_K^{-\frac{1}{2}} \|\nabla(\chi - \mathbf{I}_{S,h}^K \chi) \cdot \mathbf{n}_\Sigma\|_{0,e} + \sum_{K \in \mathcal{T}_h(\Omega_D)} \|G_h^K - G^K\|_{(\Psi_h(K))'} \right). \end{aligned}$$

Hence, the local trace inequality in [11, Lemma 6.4] leads to

$$\begin{aligned} \|\check{\mathbb{F}}_h(\xi_h)\|_{\Xi'_h} &\lesssim \max \left\{ 1, \mu, \frac{\mu\alpha}{\sqrt{\kappa}} \right\} \left(\sum_{K \in \mathcal{T}_h(\Omega_S)} [|\chi - \mathbf{I}_{S,h}^K \chi|_{2,K} + |\chi - \Pi_2^{\nabla^2, K} \chi_h|_{2,K}] \right. \\ &\quad + \sum_{K \in \mathcal{T}_h(\Omega_S)} [h_K^{-1} |\chi - \mathbf{I}_{S,h}^K \chi|_{1,K} + |\chi - \mathbf{I}_{S,h}^K \chi|_{2,K}] \\ &\quad + \sum_{K \in \mathcal{T}_h(\Omega_D)} [h_K^{-1} \|\varphi - \mathbf{I}_{D,h}^K \varphi\|_{0,K} + |\varphi - \mathbf{I}_{D,h}^K \varphi|_{1,K}] \\ &\quad \left. + \sum_{K \in \mathcal{T}_h(\Omega_S)} \|F_h^K - F^K\|_{(\Xi_h(K))'} \right), \\ \|\check{\mathbb{G}}_h(\psi_h)\|_{\Psi'_h} &\lesssim \max \{1, \kappa\} \left(\sum_{K \in \mathcal{T}_h(\Omega_D)} [|\varphi - \mathbf{I}_{D,h}^K \varphi|_{1,K} + |\varphi - \Pi_1^{\nabla, K} \varphi_h|_{1,K}] \right. \\ &\quad \left. + \sum_{K \in \mathcal{T}_h(\Omega_S)} [h_K^{-1} |\chi - \mathbf{I}_{S,h}^K \chi|_{1,K} + |\chi - \mathbf{I}_{S,h}^K \chi|_{2,K}] + \sum_{K \in \mathcal{T}_h(\Omega_D)} \|G_h^K - G^K\|_{(\Psi_h(K))'} \right). \end{aligned}$$

The estimate follows by putting together the inequality above with the Poincaré inequality and the triangle inequality

$$e_h \leq \|(\chi_h - \mathbf{I}_{S,h} \chi, \varphi_h - \mathbf{I}_{D,h} \varphi)\| + \|\chi - \mathbf{I}_{S,h} \chi, \varphi - \mathbf{I}_{D,h} \varphi\|.$$

□

We finalise this section by providing the convergence rates for the proposed VEM scheme (cf. Section 3).

Theorem 3 (convergence rates) *Under the assumptions of Lemma 8, assume further that for $\delta \in (0, 1]$, $\chi \in \mathbf{H}^{2+\delta}(\Omega_S) \cap \mathbf{H}_{T_S}^2(\Omega_S)$ and $\varphi \in \mathbf{H}^{1+\delta}(\Omega_D) \cap \mathbf{H}_*^1(\Omega_D)$. Then, the following estimate holds:*

$$e_h \lesssim \max \left\{ 1, \mu, \kappa, \frac{\mu\alpha}{\sqrt{\kappa}} \right\} h^\delta (|\chi|_{2+\delta, \Omega_S} + |\varphi|_{1+\delta, \Omega_D} + \|\mathbf{f}\|_{0, \Omega_S} + \|g\|_{0, \Omega_D}).$$

Proof Note that Lemma 4 implies that

$$\sum_{K \in \mathcal{T}_h(\Omega_S)} \|F_h^K - F^K\|_{(\varepsilon_h(K))'} \lesssim h^\delta \|\mathbf{f}\|_{0, \Omega_S} \quad \text{and} \quad \sum_{K \in \mathcal{T}_h(\Omega_D)} \|G_h^K - G^K\|_{(\psi_h(K))'} \lesssim h^\delta \|g\|_{0, \Omega_D}.$$

Thus, a direct application of Lemmas 4 and 7 in Lemma 8 yield the result. \square

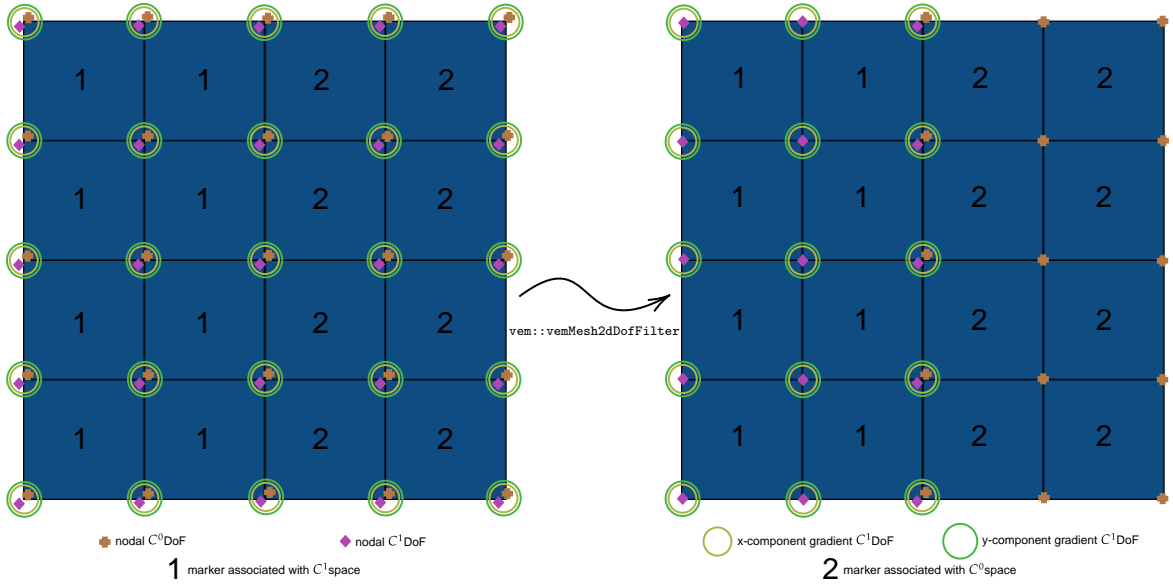


Fig. 3 Schematic overview of the filtering procedure performed by the class `vem::vemMesh2dDofFilter`. Left: A discretisation of the unit square highlighting the DoFs for both C^1 -VEM and C^0 -VEM spaces. Right: The resulting mesh after the filtering procedure, where the interface is defined by $\Sigma = \{(x, y) \in \Omega : x = \frac{1}{2}\}$ and $\Omega = (0, 1)^2$.

5 Numerical experiments

This section is devoted to numerical experiments that confirm the approximation properties and theoretical predictions established in Section 4 for the VEM scheme introduced in Section 3.

The total computational relative energy error is defined by using the local polynomial approximation of the solution as follows

$$\bar{e}_h^2 = \bar{e}_{\chi_h}^2 + \bar{e}_{\varphi_h}^2 := \frac{\sum_{K \in \mathcal{T}_h(\Omega_S)} |\chi - \Pi_2^{\nabla^2, K} \chi_h|_{2, K}^2}{\sum_{K \in \mathcal{T}_h(\Omega_S)} |\chi|_{2, K}^2} + \frac{\sum_{K \in \mathcal{T}_h(\Omega_D)} |\varphi - \Pi_1^{\nabla, K} \varphi_h|_{1, K}^2}{\sum_{K \in \mathcal{T}_h(\Omega_D)} |\varphi|_{1, K}^2}.$$

Whereas, the order of convergence $r(\cdot)$ applied to either \bar{e}_h , \bar{e}_{χ_h} , or \bar{e}_{φ_h} of the refinement $1 \leq j$ is computed from the formula

$$r(\cdot)^{j+1} = \frac{\log \left(\frac{(\cdot)^{j+1}}{(\cdot)^j} \right)}{\log \left(\frac{h^{j+1}}{h^j} \right)},$$

with h indicating the maximum element diameter in \mathcal{T}_h . In turn, the stabilisation term $S_S^K(\chi_h, \xi_h)$ follows the “diagonal recipe” introduced in [10] and $S_D^K(\varphi_h, \psi_h)$ is chosen as the well-known DOFI–DOFI stabilisation operator. We also recall that these operators are weighted by μ and κ , respectively.

The implementation has been carried out using the object-oriented C++ library VEM++ [26], which provides a new functionality to filter mesh DoFs according to element markers through the class `vem::vemMesh2dDofFilter`. The procedure starts from a mesh where multiple VEM spaces (e.g. the C^1 –VEM and C^0 –VEM spaces defined in Section 3.2 and 3.3, respectively) are simultaneously defined over the entire mesh. Each element is then assigned a marker identifying the space that must be retained on it. After applying the filter, only the DoFs associated with the selected space are kept on each marked element. Consequently, both sets of DoFs coexist only on the interface between regions with different markers. In Fig. 3, we provide a schematic overview of this process.

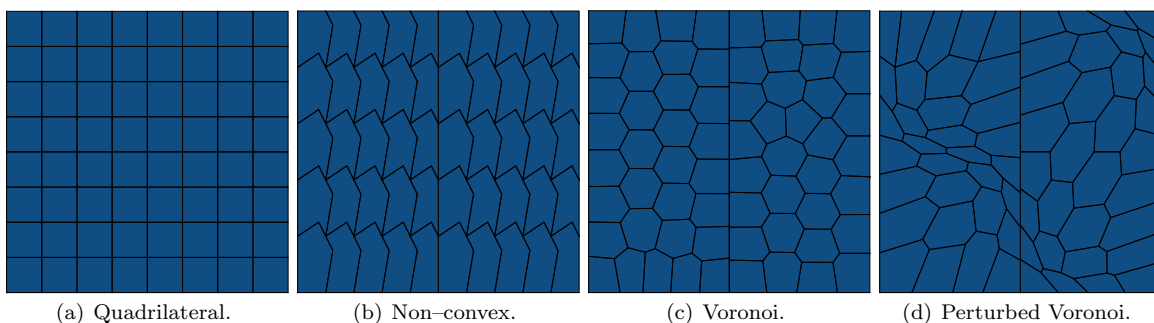


Fig. 4 Variety of discretisations used for the unit square in Experiments 1 and 2.

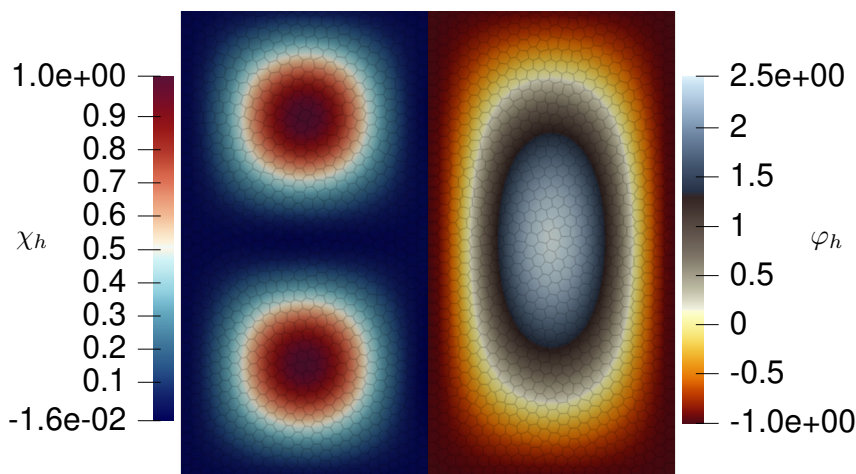


Fig. 5 Experiment 1. Nodal values of the VEM solutions χ_h and φ_h on the Voronoi mesh at the final refinement level.

5.1 Experiment 1: manufacture solution with zero value in the interface

In this experiment, we consider the domain $\Omega = (0, 1)^2$ (see Fig. 4), which is split into two subdomains: $\Omega_S = (0, \frac{1}{2}) \times (0, 1)$ and $\Omega_D = (\frac{1}{2}, 1) \times (0, 1)$. The interface between them is given by $\Sigma = \Gamma_S \cap \Gamma_D = \{(x, y) \in \Omega : x = \frac{1}{2}\}$. As illustrated in Fig. 4(c)–4(d), the computational meshes join at Σ with non-matching nodes, highlighting the scheme’s ability to handle nonconforming interfaces.

The smooth manufactured solutions are set as

$$\chi(x, y) = \frac{1}{20} \sin(2\pi x)^2 \sin(2\pi y)^2, \quad \varphi(x, y) = \varphi_0 (x-1)^2 \left(\frac{1}{2} - x\right)^2 y^2 (1-y)^2 - 1, \\ \mathbf{u}(x, y) = \mathbf{curl}(\chi(x, y)), \quad \text{and} \quad p(x, y) = 0.$$

Note that the source terms \mathbf{f} and g are sufficiently smooth, as they are derived from the prescribed manufactured solutions. In addition, the transmission conditions in (5) lead to additional functionals in the right-hand side of the system. The model parameters are set to unity ($\mu = \kappa = \alpha = 1$) and $\varphi_0 = 1.44 \times 10^4$.

The error history is reported in Table 1, where we observe an asymptotic linear decay for the scheme proposed in Section 3, as predicted by Theorem 3 for all the mesh types listed in Fig. 4. In addition, a snapshot of the nodal values for the variables of interest, which are known through the DoFs (cf. Section 3.4), are shown in Fig. 5 for the Voronoi mesh (see Fig. 4(c)) in the last refinement step.

\mathcal{T}_h	h	#DoFs	\bar{e}_h	$r(\bar{e}_h)$	\bar{e}_{χ_h}	$r(\bar{e}_{\chi_h})$	\bar{e}_{φ_h}	$r(\bar{e}_{\varphi_h})$
Quad.	6.25e-02	613	3.56e-01	*	2.77e-01	*	2.23e-01	*
	3.12e-02	2245	1.80e-01	0.99	1.39e-01	1.00	1.14e-01	0.97
	1.56e-02	8581	9.00e-02	1.00	6.94e-02	1.00	5.73e-02	0.99
	7.81e-03	33541	4.50e-02	1.00	3.47e-02	1.00	2.87e-02	1.00
Nonc.	2.83e-02	7505	1.91e-01	*	1.70e-01	*	8.88e-02	*
	2.36e-02	10805	1.62e-01	0.91	1.44e-01	0.89	7.43e-02	0.98
	2.02e-02	14705	1.41e-01	0.93	1.25e-01	0.91	6.38e-02	0.99
	1.77e-02	19205	1.24e-01	0.96	1.10e-01	0.95	5.59e-02	0.99
Vor.	4.42e-02	2131	2.60e-01	*	2.07e-01	*	1.56e-01	*
	3.12e-02	4222	1.86e-01	0.96	1.48e-01	0.97	1.12e-01	0.95
	2.21e-02	8347	1.35e-01	0.93	1.08e-01	0.90	8.01e-02	0.98
	1.56e-02	16692	9.46e-02	1.02	7.59e-02	1.03	5.65e-02	1.00
Pert.	4.42e-02	2122	3.07e-01	*	2.52e-01	*	1.76e-01	*
	3.12e-02	4224	2.27e-01	0.88	1.85e-01	0.89	1.31e-01	0.85
	2.21e-02	8347	1.63e-01	0.95	1.35e-01	0.92	9.21e-02	1.02
	1.56e-02	16659	1.18e-01	0.92	9.55e-02	0.99	6.98e-02	0.80

Table 1 Experiment 1. Convergence history of the proposed VEM for a variety of meshes.

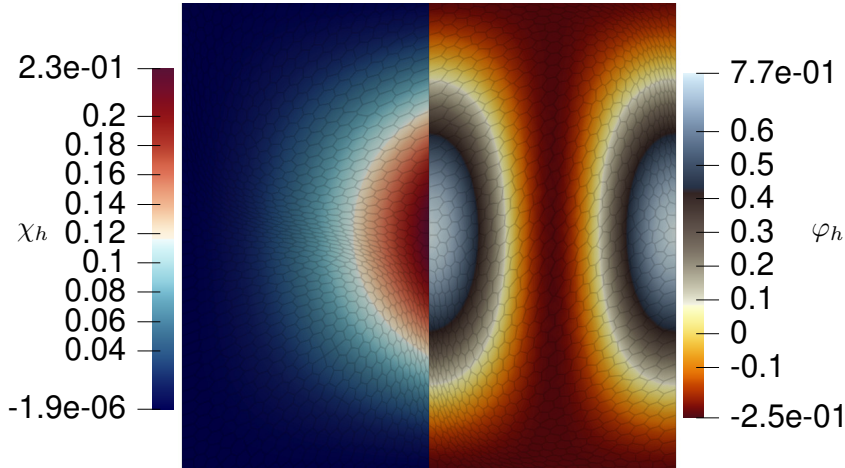


Fig. 6 Experiment 2. Nodal values of the VEM solutions χ_h and φ on the finest refinement of the perturbed Voronoi mesh.

5.2 Experiment 2: manufactured solution with nonzero value in the interface

We now extend the result observed in Experiment 1. Following the same domain configuration and unit parameter settings (cf. Section 5.1), we adopt a manufactured solution that does not satisfy the transmission conditions (5). Consequently, additional right-hand side forcing terms are introduced to

compensate for this mismatch. Such a manufactured solutions are given by

$$\begin{aligned}\chi(x, y) &= \sin(x)^2 \sin(\pi y)^2, & \varphi(x, y) &= \sin(\pi y)^2 \cos(2\pi x)^2 - \frac{1}{4}, \\ \mathbf{u}(x, y) &= \mathbf{curl}(\chi(x, y)), & \text{and } p(x, y) &= \sin(\pi y) \cos(2\pi x).\end{aligned}$$

Table 2 reports the error history for the VEM scheme proposed in Section 3. Once again, the expected linear order of convergence is observed (cf. Theorem 3) for all polygonal meshes considered (see Fig. 4). Moreover, the nodal values of the VEM solutions χ_h and φ_h are shown in Fig. 6 for the Perturbed Voronoi mesh (see Fig. 4(d)) in the last refinement step.

\mathcal{T}_h	h	#DoFs	\bar{e}_h	$r(\bar{e}_h)$	\bar{e}_{χ_h}	$r(\bar{e}_{\chi_h})$	\bar{e}_{φ_h}	$r(\bar{e}_{\varphi_h})$
Quad.	6.25e-02	613	2.56e-01	★	1.26e-01	★	2.23e-01	★
	3.12e-02	2245	1.29e-01	0.99	6.30e-02	1.00	1.12e-01	0.99
	1.56e-02	8581	6.44e-02	1.00	3.15e-02	1.00	5.62e-02	1.00
	7.81e-03	33541	3.22e-02	1.00	1.57e-02	1.00	2.81e-02	1.00
Nonc.	2.83e-02	7505	1.35e-01	★	1.04e-01	★	8.65e-02	★
	2.36e-02	10805	1.12e-01	1.03	8.61e-02	1.05	7.21e-02	1.00
	2.02e-02	14705	9.53e-02	1.07	7.26e-02	1.11	6.18e-02	1.00
	1.77e-02	19205	8.24e-02	1.09	6.22e-02	1.16	5.41e-02	1.00
Vor.	4.42e-02	2131	1.91e-01	★	1.12e-01	★	1.55e-01	★
	3.12e-02	4222	1.39e-01	0.91	8.51e-02	0.79	1.10e-01	0.97
	2.21e-02	8347	9.76e-02	1.03	5.74e-02	1.13	7.89e-02	0.97
	1.56e-02	16692	6.96e-02	0.97	4.23e-02	0.88	5.53e-02	1.02
Pert.	4.42e-02	2122	2.22e-01	★	1.35e-01	★	1.77e-01	★
	3.12e-02	4224	1.60e-01	0.95	9.63e-02	0.97	1.28e-01	0.93
	2.21e-02	8347	1.11e-01	1.06	6.71e-02	1.04	8.83e-02	1.07
	1.56e-02	16659	8.16e-02	0.88	5.03e-02	0.83	6.43e-02	0.91

Table 2 Experiment 2. Convergence history of the proposed VEM for a variety of meshes.

5.3 Experiment 3: quarter annulus dead-end filter

One important application involving coupled free-flow and porous flow is the dead-end filtration process. The design of these filtration systems plays a significant role in several industries, including the chemical, pharmaceutical, and aeronautical sectors [35].

Following [43], we consider the computational domain shown in Figure 7 where the free-flow region is defined as $\Omega_S = \{(x, y) \in \mathbb{R}^2 : 4 < x^2 + y^2 < 9, x > 0, y > 0\}$, while the porous medium occupies the region $\Omega_D = \{(x, y) \in \mathbb{R}^2 : 1 < x^2 + y^2 < 4, x > 0, y > 0\}$, and the interface separating both regions is given by $\Sigma = \{(x, y) \in \mathbb{R}^2 : x^2 + y^2 = 4, x \geq 0, y \geq 0\}$.

The boundary conditions imposed on the viscous fluid are prescribed in terms of the velocity field, as follows

$$\mathbf{u}(x, y) = \begin{cases} \left(-\frac{x}{30}, -\frac{y}{30}\right) & \text{on } \Gamma_{S,1}, \\ \left(-\frac{1}{10}, 0\right) & \text{on } \Gamma_{S,2}, \\ \left(0, -\frac{1}{10}\right) & \text{on } \Gamma_{S,3}. \end{cases}$$

Here, the boundary sections are given by the sets $\Gamma_{S,1} = \{(x, y) \in \mathbb{R}^2 : x^2 + y^2 = 9, x \geq 0, y \geq 0\}$, $\Gamma_{S,2} = \{(x, y) \in \mathbb{R}^2 : 2 \leq x \leq 3, y = 0\}$, and $\Gamma_{S,3} = \{(x, y) \in \mathbb{R}^2 : 2 \leq y \leq 3, x = 0\}$. Notice that from the definition of a stream function, we have the relation $\mathbf{u} = \mathbf{curl} \chi$. Thus,

$$\chi(x, y) = \begin{cases} \frac{3}{10} \arctan\left(\frac{y}{x}\right) & \text{on } \Gamma_{S,1}, \\ 0 & \text{on } \Gamma_{S,2}, \\ \frac{3\pi}{20} & \text{on } \Gamma_{S,3}. \end{cases} \quad \text{and} \quad \nabla \chi(x, y) = \begin{cases} \left(-\frac{y}{30}, \frac{x}{30}\right) & \text{on } \Gamma_{S,1}, \\ \left(0, \frac{1}{10}\right) & \text{on } \Gamma_{S,2}, \\ \left(-\frac{1}{10}, 0\right) & \text{on } \Gamma_{S,3}. \end{cases}$$

prescribe the boundary conditions for the stream function on $\Gamma_{S,1} \cup \Gamma_{S,2} \cup \Gamma_{S,3}$. On the other hand, no flux boundary conditions are prescribed on $\Gamma_{D,2} = \{(x, y) \in \mathbb{R}^2 : 1 \leq x \leq 2, y = 0\} \cup \{(x, y) \in \mathbb{R}^2 : 1 \leq y \leq 2, x = 0\}$ and zero Darcy's pressure is given on $\Gamma_{D,1} = \{(x, y) \in \mathbb{R}^2 : x^2 + y^2 = 1, x \geq 0, y \geq 0\}$. Moreover, thanks to the mixed boundary conditions imposed for φ , we seek the solution in the space $H_{\Gamma_{D,1}}^1(\Omega_D) := \{\psi \in H^1 : \psi = 0 \text{ on } \Gamma_{D,1}\}$ and no Lagrange multipliers are required for this numerical test.

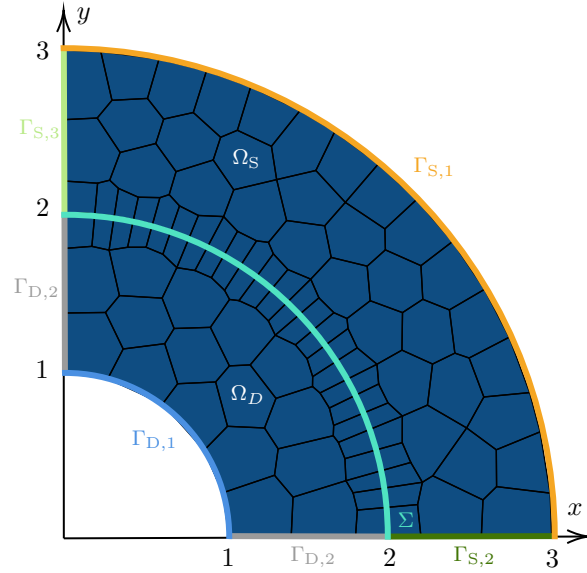
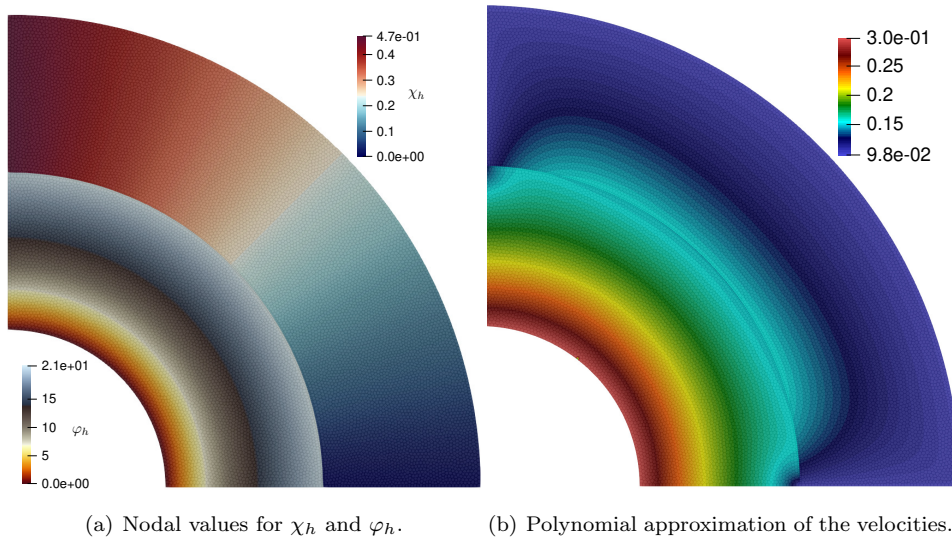


Fig. 7 Experiment 3. Domain configuration for quarter annulus dead-end filter discretised with a coarse Voronoi mesh.

Snapshots of the variables of interest are provided in Fig. 8 for a Voronoi discretisation of the mesh with 15,501 elements. In particular, Fig 8(a) shows the nodal values of χ_h and φ_h . Whereas, Fig 8(b) illustrate the local polynomial approximation of the velocities as follows: $\mathbf{curl}(\Pi_2^{\nabla^2, K} \chi_h)$ for the Stokes velocity and $\kappa \nabla(\Pi_1^{\nabla, K} \varphi_h)$ for Darcy's velocity. These fields have been smoothed by averaging the values across coincident nodes. We recall that the physical parameters for this test are set to $\mu = 1$, $\kappa = 10^{-2}$, and $\alpha = \frac{\sqrt{\kappa}}{\mu}$. The stream function – pressure formulation is able to recover the results from the simulations performed previously in [43].



(a) Nodal values for χ_h and φ_h .

(b) Polynomial approximation of the velocities.

Fig. 8 Experiment 3. Snapshots of the variables of interest for the quarter annulus dead-end filter domain discretised with 15,501 Voronoi elements.

5.4 Experiment 4: blood flow network on encapsulation-based bioartificial organs

Bioartificial organs are engineered constructs that combine living cells with biocompatible materials to reproduce, restore, or augment specific physiological functions. These systems are designed to interface with host tissues and operate as substitutes for damaged or missing organs. Their development typically relies on biocompatible scaffolds, which provide a structural environment for cell growth and tissue formation through the incorporation of cells and bioactive factors, we refer to [40,54] for more details.

A representative example is the bioartificial pancreas, where hydrogel-based scaffolds are used to encapsulate pancreatic islets containing insulin-secreting β -cells. The encapsulation device protects the pancreatic islets through filtration mechanisms provided by semi-permeable membranes [27,51].

In this experiment, we consider a different phenomena. Following [15], we model a simplified bioartificial organ of size $0.87\text{cm} \times 1.37\text{cm}$; the flow network Ω_S whose inner walls Σ act as ultrafiltration membranes for blood plasma. The blood plasma entering to the network through Γ_S^{in} with a velocity of 3.5cm/s , exits through Γ_S^{out} with a no traction condition, and no velocity is imposed for the external wall Γ_S^{ext} . The porous biocompatible scaffold medium Ω_D which avoids the fluid to scape through the external wall (i.e., no flux boundary conditions on Γ_D^{ext}) is embedded within the flow network and interacts with it through the ultrafiltration membranes Σ . Such a configuration enables the exchange of oxygen and nutrients between the blood plasma and the cells residing within the scaffold, thereby supporting the long-term viability of the transplanted cells. Fig 9 illustrates the specific domain configuration considered in this simulation, where the straight channel has a width of 0.03cm .

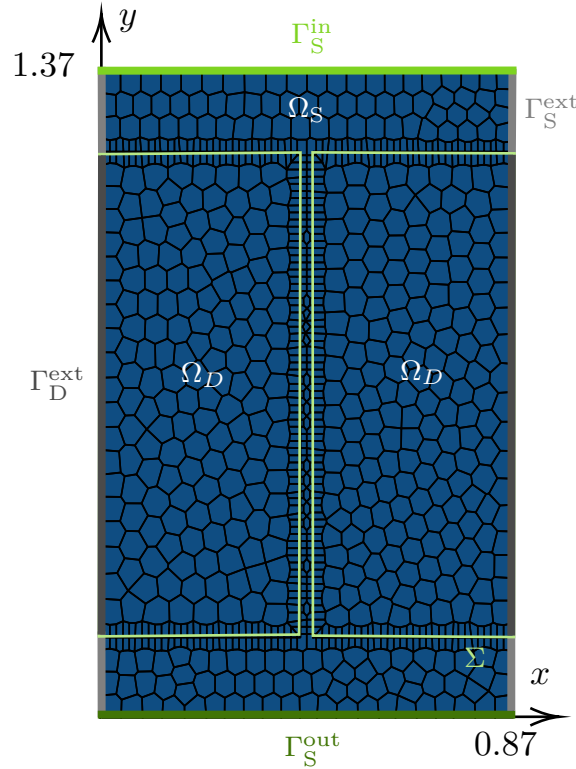


Fig. 9 Experiment 4. Blood flow network with straight channel embedded within a bioartificial scaffold domain discretised with a coarse Voronoi meshes.

Regarding the physical parameters, the blood viscosity constant is fixed to $\mu = 4 \times 10^{-2} \frac{\text{g}}{\text{cm s}}$, the slip coefficient is set to $\gamma = 10^3 \frac{\text{g}}{\text{cm}^2 \text{s}}$, and we explore the influence of the permeability constant by varying its values, i.e., $K \in \{10^{-7}, 10^{-4}, 10^{-1}, 10^2\}$ with units $\frac{\text{cm}^3 \text{s}}{\text{g}}$. To translate this setting to our model, we have that $\kappa = K\mu$ and $\alpha = \frac{\gamma\sqrt{\kappa}}{\mu}$. On the other hand, the stream function is set free on Γ_S^{out}

and inherits the following boundary conditions

$$\chi(x, y) = \begin{cases} 3.5x & \text{on } \Gamma_S^{\text{in}}, \\ 0 & \text{on } \Gamma_S^{\text{ext}} \cap \{(x, y) \in \mathbb{R}^2 : x = 0\}, \\ 3.5 & \text{on } \Gamma_S^{\text{ext}} \cap \{(x, y) \in \mathbb{R}^2 : x = 0.87\}. \end{cases} \quad \text{and} \quad \nabla\chi(x, y) = \begin{cases} (3.5, 0) & \text{on } \Gamma_S^{\text{in}}, \\ (0, 0) & \text{on } \Gamma_S^{\text{ext}}. \end{cases}$$

As expected, higher values of permeability allow blood to flow more freely across the interface Σ , which consequently reduces the total volumetric flow rate remaining within the straight channel. The simulations indicate that while higher permeability values can be physically accommodated by the model, the width of the channel would need to be proportionally increased to prevent excessive fluid passing through the interface. Snapshots of the computed velocity and pressure fields are provided in Figs. 10–11.

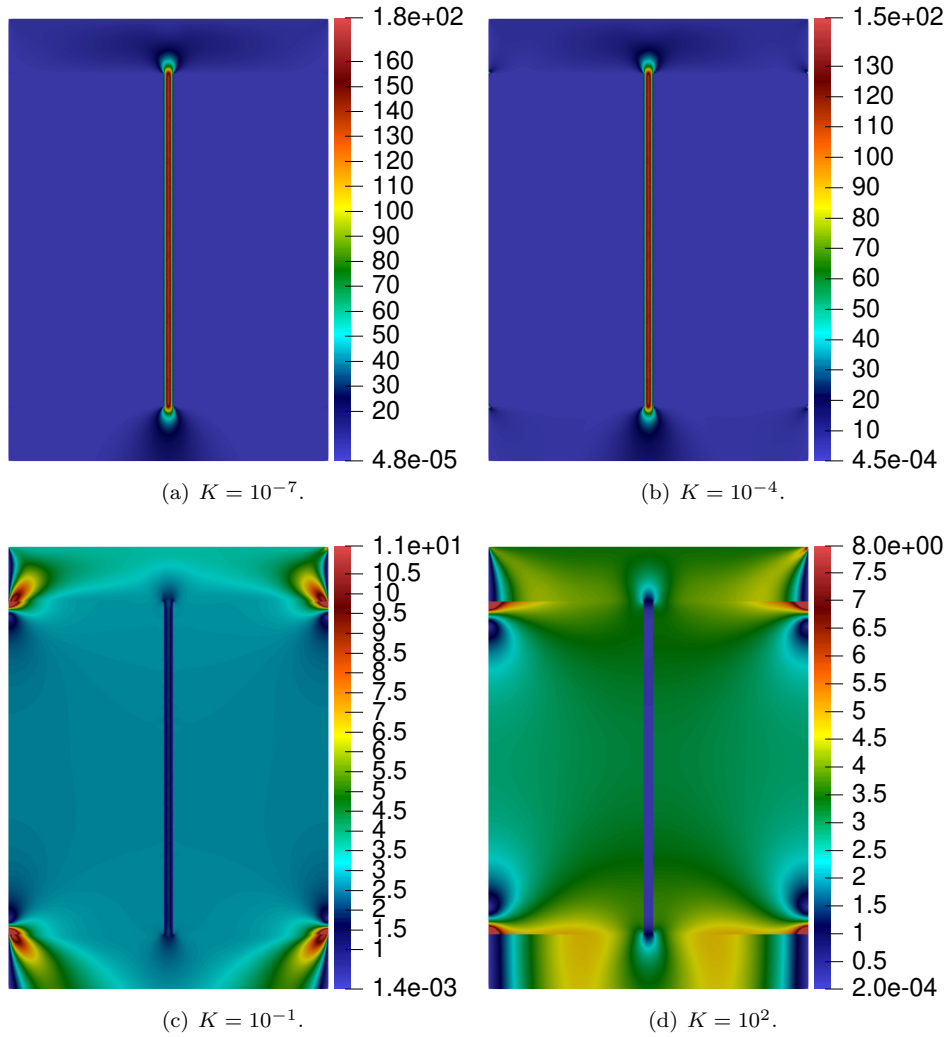


Fig. 10 Experiment 4. Stokes' and Darcy's velocities for a straight blood flow network embedded within a bioartificial scaffold domain discretised with a Voronoi meshes composed of 55,292 elements for a variety different values of K .

6 Conclusion

Several steps in the mathematical proofs presented herein posed challenges. More specifically, the seamless incorporation of transmission conditions into the stream–pressure formulation was non-trivial, in part due to the absence of stress tensors in the formulation. An advantage is that the underlying

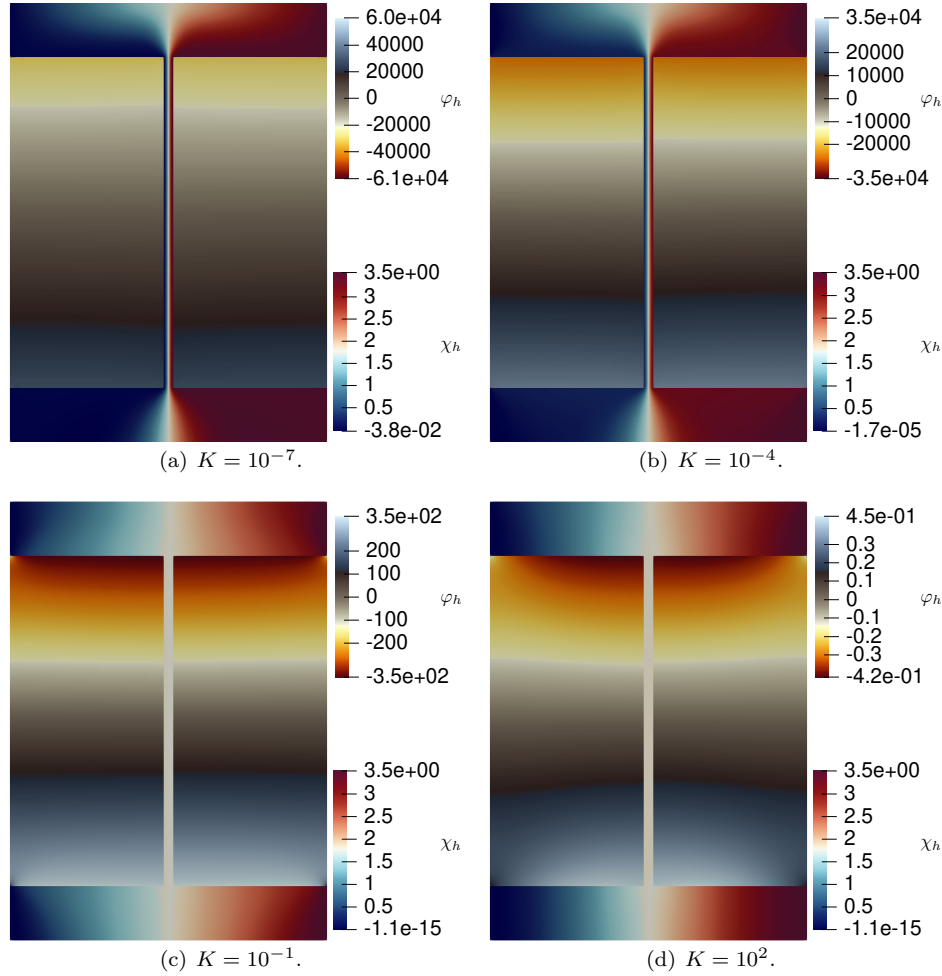


Fig. 11 Experiment 4. Nodal values of the stream function χ_h and Darcy's pressure φ_h for a straight blood flow network embedded within a bioartificial scaffold domain discretised with a Voronoi meshes composed of 55,282 elements for a variety different values of K .

structure of both the continuous and discrete problems yields a completely inf–sup-free strategy. In turn, the error analysis required the precise integration of specialised interpolation and projection operators alongside trace inequalities to yield optimal convergence rates.

Despite recent advances, extending stream-function VEM formulations to multiple connected domains remains a major open challenge. In addition, scaling this framework to a three-dimensional setting necessitates transitioning to a vector potential, which inherently demands the construction of high-order C^1 -VEM spaces for vector-valued functions. Furthermore, we are also interested in the integration of stabilisation-free techniques and the derivation of robust a posteriori error estimators, which have not yet been addressed in this context. From a geometric and computational perspective, loosening restrictive meshing assumptions, such as explicitly permitting small edges and incorporating high-order curved interfaces, represents an important direction for future research.

Funding. FD was partially supported by the European Research Council project NEMESIS (Grant No. 101115663). DM was partially supported by ANID-Chile through FONDECYT project 1261217 and by Centro de Modelamiento Matemático (CMM), FB210005, BASAL funds for centers of excellence. AER and RRB have been partially supported by the Australian Research Council through the *Future Fellowship* grant FT220100496. AER has been partially supported by the Center for Mathematical Modeling (CMM), Proyecto Basal FB210005. RRB acknowledges the support from the Center for Advanced Study (CAS) at the Norwegian Academy of Science and Letters under the program *Mathematical Challenges in Brain Mechanics*.

References

1. Adak, D., Mora, D., Silgado, A.: The Morley-type virtual element method for the Navier–Stokes equations in stream-function form. *Comput. Methods Appl. Mech. Engrg.* **419**, 116573 (2024)
2. Anaya, V., Mora, D., Reales, C., Ruiz-Baier, R.: Vorticity-pressure formulations for the Brinkman-Darcy coupled problem. *Numer. Methods Partial Differ. Equ.* **35**(2), 528–544 (2019)
3. Antonietti, P.F., Beirão da Veiga, L., Mora, D., Verani, M.: A stream virtual element formulation of the Stokes problem on polygonal meshes. *SIAM J. Numer. Anal.* **52**(1), 386–404 (2014)
4. Antonietti, P.F., Beirão da Veiga, L., Scacchi, S., Verani, M.: A C^1 virtual element method for the Cahn–Hilliard equation with polygonal meshes. *SIAM J. Numer. Anal.* **54**(1), 34–56 (2016)
5. Antonietti, P.F., Botti, M., Parolini, N., Pederzoli, V., Verani, M.: Polytopal discontinuous Galerkin discretizations of coupled non-Newtonian Stokes-Darcy systems. *arXiv preprint 2606.11935* (2026). Available at: <https://arxiv.org/abs/2606.11935>
6. Badea, L., Discacciati, M., Quarteroni, A.: Numerical analysis of the Navier–Stokes/Darcy coupling. *Numer. Math.* **115**(2), 195–227 (2010)
7. Beavers, G.S., Joseph, D.D.: Boundary conditions at a naturally permeable wall. *J. Fluid Mech.* **30**(1), 197–207 (1967)
8. Beirão da Veiga, L., Brezzi, F., Cangiani, A., Manzini, G., Marini, L.D., Russo, A.: Basic principles of virtual element methods. *Math. Models Methods Appl. Sci.* **23**(01), 199–214 (2013)
9. Beirão da Veiga, L., Brezzi, F., Marini, L.D., Russo, A.: The Hitchhiker’s guide to the virtual element method. *Math. Models Methods Appl. Sci.* **24**(08), 1541–1573 (2014)
10. Beirão da Veiga, L., Dassi, F., Russo, A.: High-order virtual element method on polyhedral meshes. *Comput. Math. Appl.* **74**(5), 1110–1122 (2017)
11. Beirão da Veiga, L., Lovadina, C., Russo, A.: Stability analysis for the virtual element method. *Math. Models Methods Appl. Sci.* **27**(13), 2557–2594 (2017)
12. Bernardi, C., Hecht, F., Pironneau, O.: Coupling Darcy and Stokes equations for porous media with cracks. *ESAIM: Math. Model. Numer. Anal.* **39**(1), 7–35 (2005)
13. Boon, W.M., Koch, T., Kuchta, M., Mardal, K.A.: Robust monolithic solvers for the Stokes–Darcy problem with the Darcy equation in primal form. *SIAM J. Sci. Comput.* **44**(4), B1148–B1174 (2022)
14. Brenner, S., Scott, R.: *The mathematical theory of finite element methods*. Springer (2008)
15. Bukač, M., Čanić, S., Muha, B., Wang, Y.: A computational algorithm for optimal design of a bioartificial organ scaffold architecture. *PLOS Comput. Biol.* **20**(11) (2024)
16. Bukač, M., Muha, B., Salgado, A.J.: Analysis of a diffuse interface method for the Stokes–Darcy coupled problem. *ESAIM: Math. Model. Numer. Anal.* **57**(5), 2623–2658 (2023)
17. Burman, E., Delay, G., Ern, A.: An unfitted hybrid high-order method for the Stokes interface problem. *IMA J. Numer. Anal.* **41**(4), 2362–2387 (2021)
18. Camaño, J., Oyarzúa, R., Rojo, K., Villa-Fuentes, S.: A mixed finite element method based on pseudostress and stream-function for the Navier–Stokes problem in 2D. Preprint 2026-13, Centro de Investigación en Ingeniería Matemática (CI²MA), Universidad de Concepción (2026). Available at: <http://www.ci2ma.udec.cl/publications/preprints/>
19. Camaño, J., Gatica, G.N., Oyarzúa, R., Ruiz-Baier, R., Venegas, P.: New fully-mixed finite element methods for the Stokes–Darcy coupling. *Comput. Methods Appl. Mech. Eng.* **295**, 362–395 (2015)
20. Cangiani, A., Georgoulis, E.H., Pryer, T., Sutton, O.J.: A posteriori error estimates for the virtual element method. *Numer. Math.* **137**, 857–893 (2017)
21. Carstensen, C., Mallik, G., Nataraj, N.: Nonconforming finite element discretization for semilinear problems with trilinear nonlinearity. *IMA J. Numer. Anal.* **41**(1), 164–205 (2021)
22. Cayco, M.E., Nicolaides, R.A.: Finite element technique for optimal pressure recovery from stream function formulation of viscous flows. *Math. Comp.* **46**(174), 371–377 (1986)
23. Chen, L., Huang, J.: Some error analysis on virtual element methods. *Calcolo* **55**(1), 5 (2018)
24. Ciminin, F., Discacciati, M.: Navier–Stokes/Forchheimer models for filtration through porous media. *Appl. Numer. Math.* **72**, 205–224 (2013)
25. D’Angelo, C., Zunino, P.: Robust numerical approximation of coupled Stokes’ and Darcy’s flows applied to vascular hemodynamics and biochemical transport. *ESAIM: Math. Model. Numer. Anal.* **45**(3), 447–476 (2011)
26. Dassi, F.: VEM++, a C++ library to handle and play with the virtual element method. *Numer. Algor.* **101**, 1633–1675 (2026)
27. Dassi, F., Khot, R., Rubiano, A.E., Ruiz-Baier, R.: Analysis and virtual element discretisation of a Stokes/Biot–Kirchhoff bulk–surface model. *Comput. Methods Appl. Mech. Eng.* **449**, 118545 (2026)
28. Discacciati, M., Miglio, E., Quarteroni, A.: Mathematical and numerical models for coupling surface and groundwater flows. *Appl. Numer. Math.* **43**(1-2), 57–74 (2002)
29. Eggenweiler, E., Discacciati, M., Rybak, I.: Analysis of the Stokes–Darcy problem with generalised interface conditions. *ESAIM: Math. Model. Numer. Anal.* **56**(2), 727–742 (2022)
30. Ervin, V., Jenkins, E.W., Sun, S.: Coupled generalized nonlinear Stokes flow with flow through a porous medium. *SIAM J. Numer. Anal.* **47**(2), 929–952 (2009)
31. Fairag, F.: Numerical computations of viscous, incompressible flow problems using a two-level finite element method. *SIAM Journal on Scientific Computing* **24**(6), 1919–1929 (2003)
32. Gatica, G., Oyarzúa, R., Sayas, F.J.: Analysis of fully-mixed finite element methods for the Stokes–Darcy coupled problem. *Math. Comp.* **80**, 1911–1948 (2011)
33. Gatica, G.N., Oyarzúa, R., Sayas, F.J.: A twofold saddle point approach for the coupling of fluid flow with nonlinear porous media flow. *IMA J. Numer. Anal.* **32**(3), 845–887 (2012)
34. Girault, V., Raviart, P.A.: *Finite Element Methods for Navier–Stokes Equations*. Springer Berlin, Heidelberg, Berlin (1986)
35. Hanspal, N.S., Waghode, A.N., Nassehi, V., Wakeman, R.J.: Numerical analysis of coupled Stokes/Darcy flows in industrial filtrations. *Trans. Porous Media* **64**(1), 73–101 (2006)
36. Huang, J., Yu, Y.: A medius error analysis for nonconforming virtual element methods for Poisson and biharmonic equations. *J. Comput. Appl. Math.* **386**, 113229 (2021)

37. Kanschat, G., Rivière, B.: A strongly conservative finite element method for the coupling of Stokes and Darcy flow. *J. Comput. Phys.* **229**(17), 5933–5943 (2010)
38. Khot, R., Mora, D., Ruiz-Baier, R.: Virtual element methods for Biot–Kirchhoff poroelasticity. *Math. Comp.* **94**(353), 1101–1146 (2025)
39. Kim, D., Pani, A.K., Park, E.J.: Morley finite element methods for the stationary quasi-geostrophic equation. *Comput. Methods Appl. Mech. Engrg.* **375**, 113639 (2021)
40. Krishani, M., Shin, W.Y., Suhaimi, H., Sambudi, N.S.: Development of scaffolds from bio-based natural materials for tissue regeneration applications: A review. *Gels* **9**(2) (2023)
41. Lippke, A., Wagner, H.: Numerical solution of the Navier-Stokes equations in multiply connected domains. *Comput. Fluids* **20**(1), 19–28 (1991)
42. Liu, J.G., Shu, C.W.: A high-order discontinuous Galerkin method for 2D incompressible flows. *J. Comput. Phys.* **160**(2), 577–596 (2000)
43. Liu, X., Li, R., Chen, Z.: A virtual element method for the coupled Stokes–Darcy problem with the Beaver–Joseph–Saffman interface condition. *Calcolo* **56**(4), 48 (2019)
44. Mishra, S., Natarajan, E.: A unified local projection-based stabilized virtual element method for the coupled Stokes–Darcy problem. *Adv. Comput. Math.* **50**(6), 106 (2024)
45. Mora, D., Reales, C., Silgado, A.: A C^1 -virtual element method of high order for the Brinkman equations in stream function formulation with pressure recovery. *IMA J. Numer. Anal.* **42**, 3632–3674 (2022)
46. Mora, D., Rivera, G., Rodríguez, R.: A virtual element method for the Steklov eigenvalue problem. *Math. Models Methods Appl. Sci.* **25**(08), 1421–1445 (2015)
47. Mora, D., Rivera, G., Velásquez, I.: A virtual element method for the vibration problem of Kirchhoff plates. *ESAIM: Math. Model. Numer. Anal.* **52**(4), 1437–1456 (2018)
48. Mora, D., Silgado, A.: Stream virtual elements for the Navier-Stokes system: Nonstandard boundary conditions and variable recovery algorithms. *SIAM J. Sci. Comput.* **47**, 207–237 (2025)
49. Qi, F., Liu, Y., Chen, R., Hu, P., Cai, X.C.: Computational modeling of the kidney hemodynamics with a coupled unsteady Stokes–Darcy model. *Int. J. Numer. Methods Biomed. Eng.* **41**(11), e70108 (2025)
50. Saffman, P.G.: On the boundary condition at the surface of a porous medium. *Stud. Appl. Math.* **50**(2), 93–101 (1971)
51. Song, S., Faleo, G., Yeung, R., Kant, R., Posselt, A.M., Desai, T.A., Tang, Q., Roy, S.: Silicon Nanopore Membrane (SNM) for islet encapsulation and immunoisolation under convective transport. *Sci. Rep.* **6**, 23679 (2016)
52. Vexler, B., Leykekhman, D., Wagner, J.: Fully discrete error analysis of finite element discretizations of time-dependent Stokes equations in a stream-function formulation. *ESAIM: Math. Model. Numer. Anal.* (2026). In press
53. Wang, G., Wang, F., Chen, L., He, Y.: A divergence free weak virtual element method for the Stokes–Darcy problem on general meshes. *Comput. Methods Appl. Mech. Eng.* **344**, 998–1020 (2019)
54. Wang, X.: Bioartificial organ manufacturing technologies. *Cell Trans.* **28**(1), 5–17 (2019)
55. Wen, J., Su, J., He, Y., Chen, H.: A discontinuous Galerkin method for the coupled Stokes and Darcy problem. *J. Sci. Comput.* **85**(2), 26 (2020)
56. Xie, X., Xu, J., Xue, G.: Uniformly-stable finite element methods for Darcy-Stokes-Brinkman models. *J. Comput. Math.* pp. 437–455 (2008)